TÉCNICO LISBOA

$CH_4 + H_2$ Flames Anchored on perforated Plates – A Thermoacoustic Analysis

Pedro Miguel Que Ye

Thesis to obtain the Master of Science Degree in

Mechanical Engineering

Supervisor: Prof. Edgar Caetano Fernandes

Examination Committee

Chairperson: Prof. José Manuel da Silva Chaves Ribeiro Pereira

Supervisor: Prof. Edgar Caetano Fernandes

Member of the Committee: Prof. Aires José Pinto dos Santos

December 2021

Para os que já partiram, mas que aqui ficam.

Acknowledgments

I thank my supervisor, Professor Edgar Fernandes, not only for the academic teachings, but also for encouraging and sparking an adoration for thermodynamics, combustion and science in general. I would've never been this fulfilled for my thesis if it wasn't for his enthusiasm. I also want to thank Dr. Sandra Dias for helping me to write this thesis and her availability to aid in the laboratory.

Many thanks need to go to my laboratory colleagues. Their curiosity, resourcefulness and high spirits made the experiments much more fun and beneficial.

Words of acknowledgement also go to the friends that I made throughout the last five years. From the ones who I met on the first week to the ones who I only met last year, many of you have been very supportive to me. A special word of recognition goes to Renato Thieleke and Ricardo Perdigão.

Of course, none of this could've been accomplished without Helena, Carla and Tózé – my second family. They have been my foundations since I was a little baby and have never stopped supporting me in every imaginable way. More than a million thanks to you!

And at last, but not least, a huge thank you to my family. They have been through my best and worst moments and in every single one of them they have guided me to the best path possible. I must admit that I am very lucky to have such family members!

This work was developed at the Thermofluids, Combustion and Energy Systems laboratory of the IN+ - Center for Innovation, Technology and Policy Research.

Resumo

Aplicações de combustão contínua são suscetíveis a instabilidades termoacústicas. Várias destas aplicações utilizam placas multiperfuradas (MPP) como estabilizadores de chama. Adicionalmente, devido às consequências das alterações climáticas, o hidrogénio tem vindo a ser promovido como combustível para utilização em sistemas de combustão. Tendo isto em consideração, esta tese foca-se nos efeitos de diferentes combustíveis e rácios de perfuração (ψ) das MPPs nas instabilidades termoacústicas.

As experiências são realizadas num queimador com comprimento de cavidade (L) variável e MPPs com diferentes ψ. Os combustíveis utilizados são de 100% C_3H_8, 100% CH_4 e 90% CH_4 + 10% H_2 em volume. Uma avaliação do nível de pressão do som (SPL), frequência e forma de chama é feita para os últimos dois combustíveis. Para complementar as experiências, um modelo matemático com o objetivo de prever instabilidades termoacústicas também é apresentado.

O enriquecimento de H_2 leva a mais instabilidades termoacústicas e frequências mais elevadas. Com o decréscimo de ψ das MPPs, as instabilidades são reduzidas à custa de limites mais ricos de lean-blowout (LBO). A análise da forma de chama demonstra que frequências mais elevadas são associadas ao encurtamento do comprimento de chama instável. O modelo matemático prevê mais instabilidades com a adição de H_2 e maiores ψ, porém os seus resultados não correspondem quantitativamente aos dados experimentais.

Palavras-chave: Instabilidades Termoacústicas, Placas Perfuradas, Hidrogénio, Metano, Rácio de Perfuração

Abstract

Continuous combustion applications are prone to thermoacoustic instabilities. In many of these applications, multiperforated plates (MPP) are used as flame stabilizers. Additionally, with recent climate change effects, hydrogen has been promoted as a fuel for combustion systems. Considering this, the present work focuses on the effects of MPP with different perforation ratios (ψ) and fuel blends on thermoacoustic instabilities.

Experiments are done in a burner with variable length cavity (L) and MPPs with different ψ. The fuels used are 100% C_3H_8, 100% CH_4 and 90% CH_4 + 10% H_2 in volume. Evaluation of the sound pressure level (SPL), frequency and flame shape is done for the last two blends. Also, a mathematical model to predict thermoacoustic instabilities is presented.

H_2 enrichment leads to more thermoacoustic instabilities and higher frequencies. With the decrease in ψ from the MPPs, these instabilities are reduced but at the cost of richer lean-blowout (LBO) limits. Flame shape analysis demonstrates that higher frequencies are associated with a shortening of the unstable length of the flame. The mathematical model predicts more instabilities with the addition of H_2 and higher ψ. However, its results are deviated from the experiments.

Keywords: Thermoacoustic Instabilities, Perforated Plates, Hydrogen, Methane, Perforation Ratio

Contents

List of Tables

List of Figures

Nomenclature

Acronyms

AFR	Air-to-fuel Ratio
FFT	Fast Fourier Transformation
FTF	Flame Transfer Function
GHG	Green House Gases
HENG	Hydrogen-enriched Natural Gas
LBO	Lean-blowout
MPP	Multiperforated Plate
NOx	Nitrogen Oxides
SLPM	Standard Litres per Minute
SPL	Sound Pressure Level

Chemical species

C_3H_8	Propane
CH_4	Methane
H_2	Hydrogen

Greek symbols

η	Radial non-dimensional coordinate
γ	Specific heats ratio
κ	Thermal conductivity
λ	Wave length
μ	Dynamic viscosity
ω	Angular frequency

ϕ Equivalence ratio

ψ Perforation ratio

ρ Density

σ Square root of the Prandtl number

τ Time delay

θ Azimuthal coordinate

φ Transfer function phase

ξ Axial non-dimensional coordinate

Others

$\mathcal{P}$ Plates' porosity

$\Re$ Real part

(v/v) In volume

Re Reynolds number

Roman symbols

$\boldsymbol{n}$ Normal vector

$\dot{m}$ Mass flow rate

A Flame surface area

c Speed of sound

C_P Heat capacity at constant pressure

C_V Heat capacity at constant volume

D Cavity's inner diameter

d_h Plate hole diameter

f Frequency

f_0 Resonant frequency of cavity

G_ω Flame transfer function gain

H Height

J_i Bessel function of the first kind for integer i

k Reduced frequency number

L Cavity length

l Plate thickness

L_i Damping process i

n_h Number of holes in each plate

P Power

p' Instantaneous pressure fluctuation

Q Volumetric flow rate

q' Instantaneous heat release rate fluctuation

r Radius

s Shear wave number

S_a Hexagonal area of perforation

S_f Cross-sectional area of perforation

S_L Laminar flame speed

T Period of oscillation

t Time

u Axial velocity component

u' Instantaenous velocity fluctuation

V Resonator's volume

x Axial coordinate

z Impedance

Subscripts

∞ Surrounding air conditions

ac Acoustic component

cv Convective component

$driv$, $diss$ Driving, dissipative components

ext External conditions

f Flame component

max, min Maximum, minimum

u, b Unburnt, burnt gases

Chapter 1

Introduction

Application of combustion systems can be found anywhere from propulsion to cooking, passing through heating, power generation and even military weapons. In stable combustion applications instability problems arise and these are an important subject in the field of combustion studies. Their dynamics not only include the study of reacting flow sciences, such as kinetics, transport, fluid mechanics and thermodynamics, but also requires careful analysis of acoustics, dynamical systems and control theory. These last fields are especially important to study a specific type of instability, which is the spotlight of this thesis: Thermoacoustic Instabilities.

1.1 Motivation and Literature Review

Thermoacoustic instabilities are one type of combustion instabilities which can develop spontaneously in an intrinsic way [1] or forced by natural or artificial sources, both resulting from the coupling of flame and burner dynamics. This phenomena can occur in both closed volume burners such as gas turbines and rocket engines [2] (see figure 1.1) or in open flame configurations like water heaters, stove tops and textile dryers [3, 4].

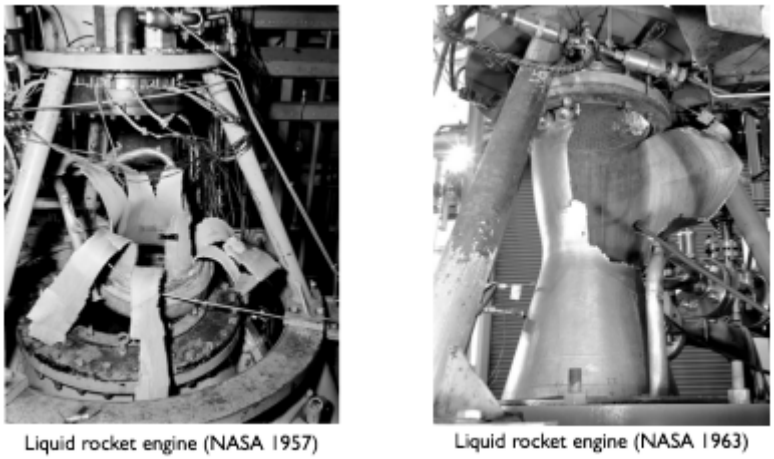

Liquid rocket engine (NASA 1957) Liquid rocket engine (NASA 1963)

Figure 1.1: Liquid rocket engine failures at NASA test facility in the Apollo Era from thermoacoustic instabilities [5].

Although these applications can have different operation modes, they can be limited by thermoacousitc instabilities which are often expressed in the form of noise and low intensity vibrations. In some cases, the oscillations can be high and continue through a long time, reducing the components life time or lead to complete failure of the systems such as liquid rocket engines [6].

If there is unsteady combustion and acoustic waves propagating in the system, the coupling between them can lead to thermoacoustic combustion instabilities. These happen when resonance, *i.e.* oscillations at frequencies with the highest amplification factor, occurs. When there is a pressure wave emitted by the surroundings or by the flame heat release, the oscillation might be amplified by the cavity, generating a perturbation in the feeding flow. Consequently if the perturbation is in phase with the flame it will enhance its oscillation creating a feedback loop (see figure 1.2) and therefore, developing self-sustained instabilities.

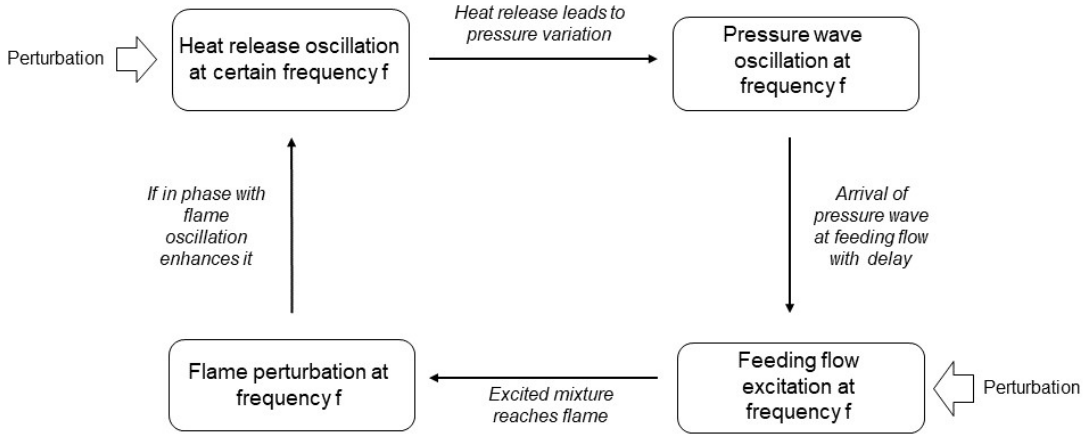

Figure 1.2: Feedback loop mechanism between flame and flow oscillation which leads to self-sustained thermoacoustic instabilities.

The criterion which leads to combustion instabilities and consequently to the sound generation was first documented by Rayleigh [7] in 1878:

> ”If heat be given to the air at the moment of greatest condensation, or be taken from it at the moment of greatest rarefaction, the vibration is encouraged. On the other hand, if heat be given at the moment of greatest rarefaction, or abstracted at the moment of greatest condensation, the vibration is discouraged.”

Meaning that for resonance to be encouraged, the system needs to be fed energy when the working fluid is expanding and removed energy when it is compressing, doubling down on the effects of expansion and compression, which consequently enhances the oscillation’s amplitude.

The flame is not the only way to generate this sound. Rijke [8] demonstrated that a tube with a heated gauze may create the ”whistling” sound which is caused by the coupling between the tube acoustics and the gauze heat release [9]. Nevertheless, the situation with the flame as the heat source is prone to higher energy releases and the effects of the instabilities are more dangerous.

A mathematical representation of the Rayleigh criterion was first introduced by Putnam and Dennis

[10] in 1953 as follows:

$$\int p'(t)q'(t)dt > 0 \tag{1.1}$$

with p' and q' as the instantaneous pressure fluctuation and heat release rate respectively. The equation 1.1 can be interpreted physically as the thermal expansion from the heated gas amplifying the pressure wave, if the latter is in phase. However, this formulation does not take into account the acoustic loss through viscous dissipation. Additionally, heat release is not only a function of time, but also of space. Considering this, Zinn [11] formulated a more appropriate equation for the criterion:

$$\int_V \int_T p'(x,t)q'(x,t)dtdV \geq \int_V \int_T L_i(x,t)dtdV \tag{1.2}$$

with V as the volume of the resonator, T as the period of the oscillations and L_i the i^{th} damping process, such as viscous fluid dissipation, heat transfer losses, conversion to kinetic turbulent energy and acoustic radiation.

Studies of unstable conical flames have been done in unconfined configurations [12–15]. It was noted that the frequencies which the thermoacoustic instabilities oscillated were close to the resonant cavity frequencies f_0 with a saw-tooth behaviour as a function of the cavity length L. Like the present thesis, these studies were performed with multiperforated plates (MPP) as stabilizers.

Noiray *et al.* [12, 13] developed an analytical model that represents the frequency behaviour with respect to the cavity length for cases with flame and without flame. Figure 1.3 shows the results obtained in [12] for a MPP with 30 mm thickness, 2 mm hole diameter and 420 holes. The model's frequency results are shown in dashed lines, while the experimental results are shown by the dots and the solid line represents the experimental sound pressure level. In the same study, the thermoacoustic instabilities were shown through the flame shape demonstrated in figure 1.4, where the figure 1.4(a) is the stable flame and figures 1.4(b)-(f) represent a cycle of one oscillation where thermoacoustic instabilities are present.

Furthermore, Ferreira [15] has made a study where the separation between perforations (perforation ratio) was considered through a factor of impedance given by Maa [16] and found that it influences the results. Although the holes radii and porosity were kept the same, *i.e.* the same number of perforations and the same ratio of perforated area and non-perforated area between plates, the results were different. They lead to great agreement between the experimental and analytical results as shown in figure 1.5, demonstrating a great influence of perforation ratio.

Studies about thermoacoustic instabilities without MPPs as stabilizers have also been done [4, 17, 18]. Durox *et al.* [4] analysed self-induced instabilities of a premixed jet flame impinging on a plate and found that strong instabilities may occur when a premixed flame impinges on a flat surface. The burner itself acts like a Helmholtz resonator but the fundamental oscillations frequency depend on the burner-to-surface distance as shown in figure 1.6.

Following the previous mentioned study, Fernandes and Leandro [17] also studied thermoacoustic instabilities of premixed flames impinging on a flat surface. A theoretical expression was deduced for the time delay of the oscillations, showing a relationship between the oscillations frequency, burner acoustic

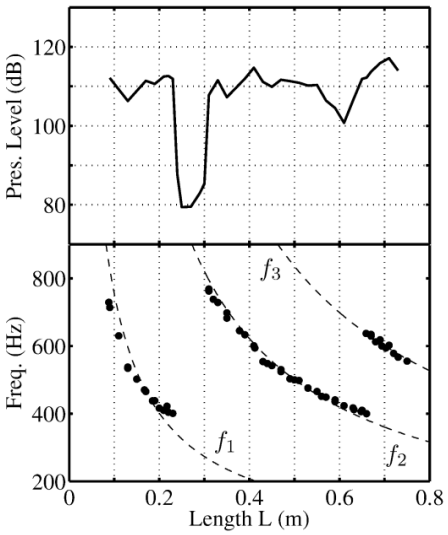

Figure 1.3: Results given by Noiray *et al.* [12]. Experiments done with a pre mixture of methane and air. Dashed lines are theoretical frequencies from the model and dots are the experimental results. $\phi = 0.86$, $\dot{m} = 5.4\,\mathrm{g\,s^{-1}}$

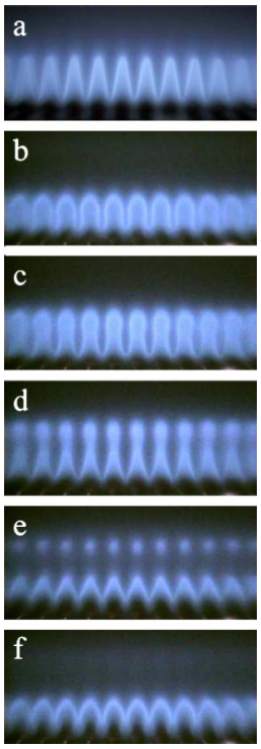

Figure 1.4: Instantaneous flame images from Noiray *et al.* [12]. (a) Stable flame regime. (b)-(f) Unstable flame regime. The images are taken at equally spaced instants and oscillations were at frequency $f = 744\,\mathrm{Hz}$.

characteristics and time delay.

Schuller *et al.* [18] studied the thermoacoustic instabilities of laminar premixed flames stabilized over an annular burner. Different flame shapes were studied (see figure 1.7) and it was found that for low flowrates, the conical and ”M” flames are stable, while at relatively higher flowrates, the ”M” and ”V” flames are stable. If the flames are perfectly stable no sound is emitted, but for certain conditions it is

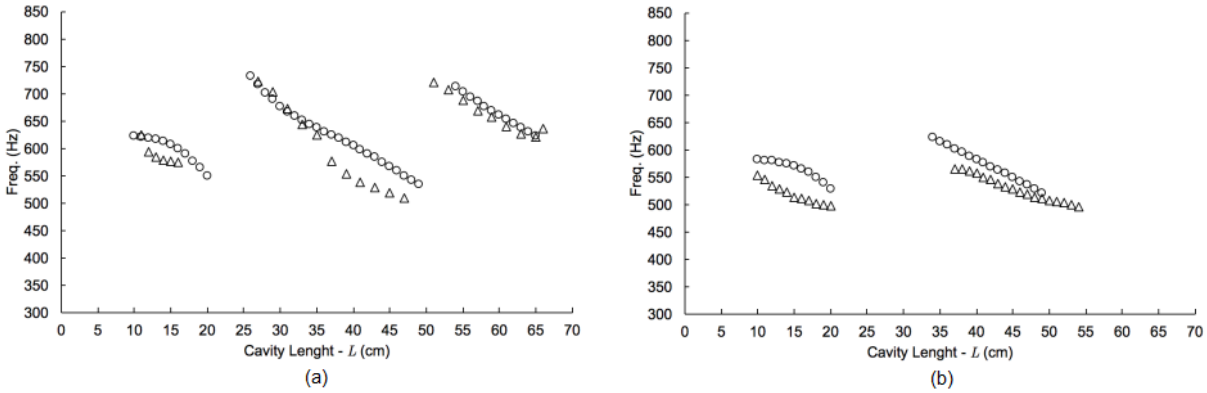

Figure 1.5: Experimental and theoretical model results by Ferreira [15]. (△) are the experimental results and (◯) are the model's results. Results in (a) are done in a MPP with higher separation between holes than (b).

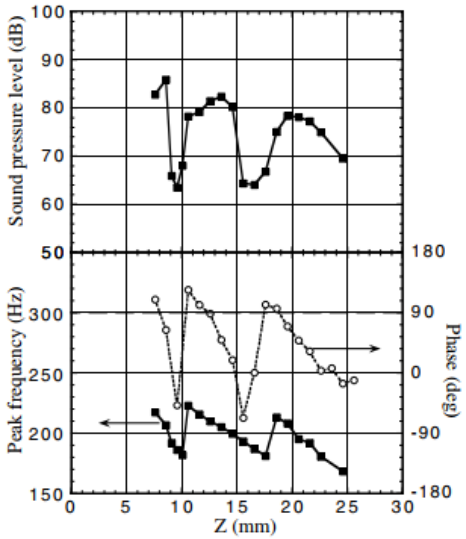

Figure 1.6: Results of sound pressure level (SPL), peak frequency and phase of the thermoacoustic instabilities from an impinging flame by Durox *et al.* [4]. Z is the burner-to-surface distance.

possible to hear an intense sound associated with an organized motion of the flame. From analysis of the flame shape when oscillations occur (see figure 1.8) it is understood that the fundamental frequency of the noise emitted by the flame always corresponds to the flame front's frequency of oscillation.

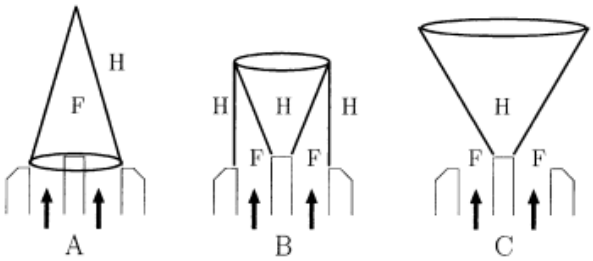

Figure 1.7: Different flame shapes studied by Schuller *et al.* [18]. (A) Conical flame, (B) "M" flame, (C) "V" flame. Regions of fresh mixture (F) and hot products (H) are shown.

Analytical modelling of the thermoacoustic instabilities was also made in the previous mentioned

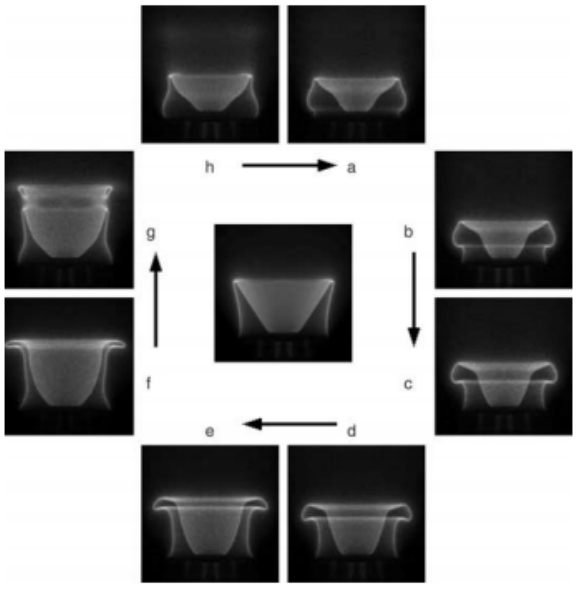

Figure 1.8: Views of the ”M” flame done by Schuller *et al.* [18]. Middle is the stable flame. (A-H) Unstable regime with oscillations at frequency $f = 138$ Hz.

studies. For that it is required to use methods that characterize the flame response to velocity oscillations. One of those methods is the Flame Transfer Function (FTF), which is also used in this thesis. In the FTF method, the flame is interpreted as an interface that separates the unburned and burned mixture represented through the G-equation, where the flame front consumes the unburned gases located at $G < 0$ (see figure 1.9) by moving in the normal direction to the flame front at the rate defined by the laminar flame speed (S_L). The flame front ($G = 0$) is also convected by the fresh mixture velocity $\boldsymbol{v}$ and yields the following equation [19]:

$$\frac{\partial G}{\partial t} + \boldsymbol{v} \cdot \nabla G = S_L \left| \nabla G \right| \tag{1.3}$$

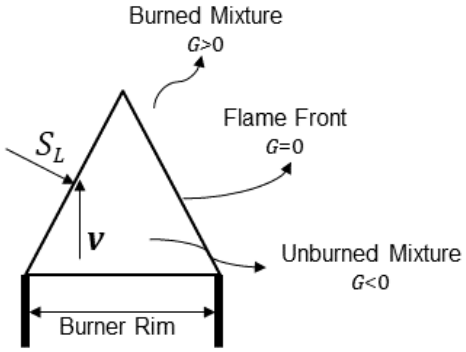

Figure 1.9: Representation of the G scalar through a conical flame.

Then the heat release rate of the oscillating flame is related to the imposed velocity through a transfer function:

$$FTF(\omega) = \frac{q'/\bar{q}}{u'/\bar{u}} \tag{1.4}$$

where q' is the instantaneous heat release fluctuation and u' is the instantaneous velocity fluctuation.

The ratio between heat release rate and mean flow velocity $\bar{q}/\bar{u}$ is introduced in order to normalize the flame transfer function and make it dimensionless. This way, the FTF relates the heat release oscillations with the velocity oscillations at a certain frequency ω.

The previous mentioned studies were realized with methane (CH_4) and propane (C_3H_8) as fuel. However, due to climate change problems recent efforts have been made to reduce the amount of green house gases (GHG) emitted to the atmosphere like the Paris Agreement of 2015, which has a collaboration of 197 countries worldwide in limiting global warming to below 2, preferably to 1.5 degrees Celsius, compared to pre-industrial levels [20]. To reach such goals, the use of hydrogen (H_2) has been proposed and promoted to use in current applications, since it is a gas that has no carbon derivatives associated to its combustion emissions.

As a consequence, H_2 application in gas turbines have been tried and researched [21]. However, its application can have undesired effects in nitrogen oxides (NOx) emissions, leading to studies on the subject [22–24]. Lantz *et al.* [22] studied the influence of H_2 addition up to 80% in volume on NOx formation and found that compared to the baseline of natural gas composition, the NOx emissions increase with H_2 addition, reaching 50% increase of NOx emissions when using 80% H_2. The reasoning for the results are the locally high temperature flames, non-perfect mixing, and reduced mixing of the reacted gases into the flame zone.

Notwithstanding the previous study, ways to reduce NOx emissions with H_2 use have been achieved. Griebel *et al.* [23] found that H_2 extends the lean-blowout limit (LBO) which in turn reduces the firing temperature, leading to lower NOx emissions. Values up to 35% reduction were reached when compared to pure CH_4 flames, even though for $\phi < 0.5$ the difference found in NOx emissions reduction between CH_4 and CH_4+H_2 flames was negligible.

Runyon [24] concluded that in practical applications, the addition of H_2 increases the reactivity and thermo-diffusive effects of the mixture, which in turn allow a stable and low NOx operation of gas turbines. Additionally, the same study proposed a power law correlation which predicts a reduction of almost 50% in combustion noise amplitudes by mixing up to 15% H_2 in CH_4.

Other applications of H_2 on jet flame burners have been studied, indicating that CH_4+H_2 blends can be used in burners initially designed for CH_4 [25]. Additionally, simple correlations for blow-out in premixed hydrogen-enriched natural gas (HENG) systems have been deduced, providing an aid in designing new HENG burners or modifying already existing ones [26].

Moreover, H_2 has also been studied in the field of thermoacoustic instabilities [27–29]. Lim *et al.* [27] made a numerical analysis of hydrogen enriched flames and found that it would enhance vibrations at higher frequencies and change the flame shape. Karlis *et al.* [28] made experimental studies on the effects of H_2 enrichment on gas turbine combustors and found that the addition of H_2 up to 10% leads to higher flammability limits, *i.e.* leads to blowout at lower equivalence ratios, but if its content is further increased random bursts of dynamic pressure and heat release start to appear. Kim *et al.* [29] found that a shift to higher resonance modes were associated with an increase of H_2 in the fuel mixture.

1.2 Scope of the Work

In this thesis, the onset of thermoacoustic instabilities is analysed for different configurations of the studied burner. Effects of the geometry of stabilizing plates, ϕ and flow speeds are evaluated. From these experiments maps of flame stability are created, showing the LBO limit and where thermoacosutic instabilities are prevalent. This is accompanied by an analysis of high-speed videos of flames at certain working conditions.

An analysis with the variation of the burner's length is also done, showing when the oscillations appear and what are their frequencies. This is coupled with the mathematical model's results to evaluate its viability and performance. The model has the objective of predicting the onset of thermoacoustic instabilities and aiding in the design and projection of future burners.

On top of those results, the addition of H_2 is also studied with the objective of understanding how the new fuel affects the system, finding its suitability to apply in current configurations or a necessity to design new ones.

1.3 Thesis Outline

This thesis is divided in 5 chapters, which are themselves organized in different subchapters. As a whole, the thesis introduces the subject studied, presents the experimental setup and its procedures, followed by the description of a mathematical model used. After that the results of experiments and model are shown and, finally, a conclusion summarising the whole work is exposed. A brief description of the chapters is presented below:

- Chapter 1, Introduction – presents an introductory text to the subject studied in this thesis, including the motivation for this work accompanied by a literary review. The objectives of this work are also presented.
- Chapter 2, Experimental Setup and Procedures – exposure of the burner configuration studied with description of the material used. Procedures and equipment used for data acquisition are also shown.
- Chapter 3, Mathematical Models – exposure of the mathematical model used for the burner acoustics and flame model. Completion of the model is done through an energy balance.
- Chapter 4, Results – demonstration and discussion of the results obtained. Flame stability maps, effects of hydrogen and analysis of flame oscillations are shown with evaluation of the mathematical model.
- Chapter 5, Conclusions – summary of the work done, referring to key findings and suggestions for future work.

Chapter 2

Experimental Setup and Procedures

The experimental setup is composed by the burner system itself and the data acquisition tools. Multiple experiments were done to study the different geometrical configurations, fuels blends, unstable flames oscillations and sound generated. The burner was studied with not only different cavity lengths, but also different stabilizing plates. This chapter first presents the burner setup, including the plates and mixture feeding system. After that the tools and procedures used to acquire data are exposed. An example of the configuration with flames can be found in figure 2.1.

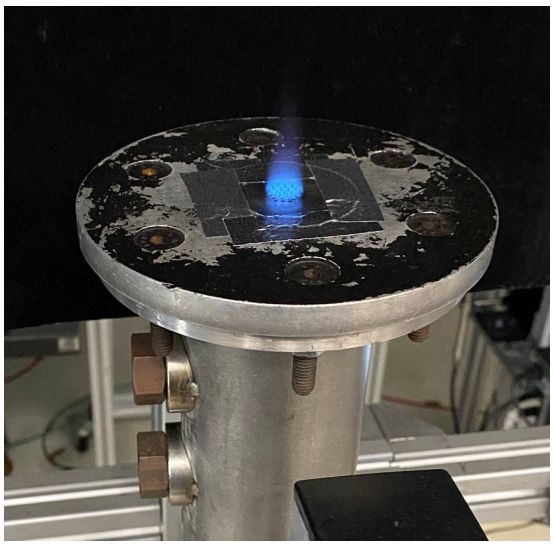

Figure 2.1: Example of configuration used for the experiments done in this thesis. Burner with plate I mounted.

2.1 Experimental Setup

2.1.1 Burner

The experiments done in this thesis are based on a burner geometry where small conical flames are anchored on thin perforated plates. Additionally, the burner has a cavity with variable length and a

premixed injection system.

A schematic of the burner configuration can be found in figure 2.2. The fuel and air are injected into the premixing pipe (1). The mixture reaches the burner cavity through twelve orifices equally spaced around the piston head (2), which has 42 mm of diameter. After the mixture exits the orifices, it flows through the variable length cavity (3) with an inner diameter of 43.5 mm and ends at the MPP (4) where the flames are anchored. The burner cavity is varied from 6 cm to 45 cm in the experiments performed for this work. The piston head is flat, which provides a quasi-perfect acoustical reflection boundary and the gap between the piston and cavity diameters is covered by a Teflon O-ring.

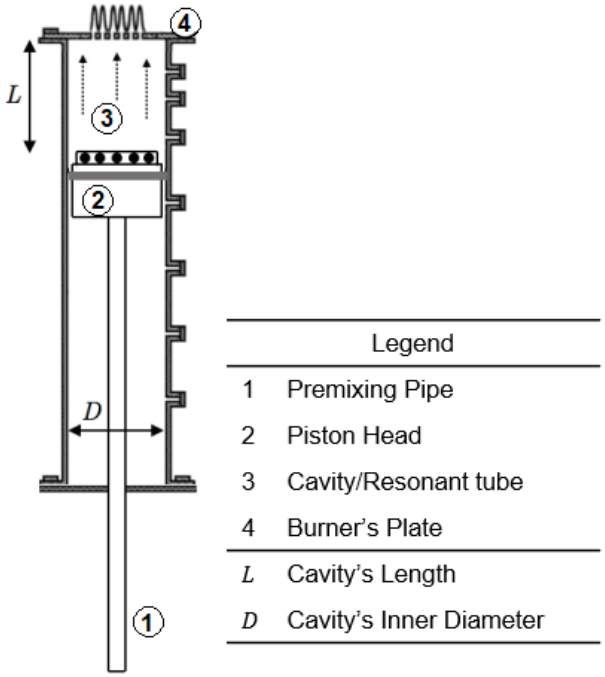

Figure 2.2: Burner configuration with its components.

2.1.2 Stabilizing Multiperforated Plates

Five burner plates (see figure 2.3) are analysed, these are made from stainless steel and a thickness of 0.5 mm. Each plate has 19 holes of 1.5 mm diameter, all with porosity $\mathcal{P} = 2.3\%$ but different perforation ratios (ψ). The perforation ratio is a parameter given as follows:

$$\psi(\%) = \frac{S_f}{S_a} \approx 90.69(\frac{2r_h}{b})^2 \tag{2.1}$$

where S_f, S_a (see figure 2.4), r_h and b are the cross-sectional area of perforation, hexagonal area of perforation, hole radius and distance between the centre of the holes respectively. Table 2.1 summarizes the burner and plate parameters. Each side of the plate has slightly different effective hole diameters, more details are found in Appendix A.

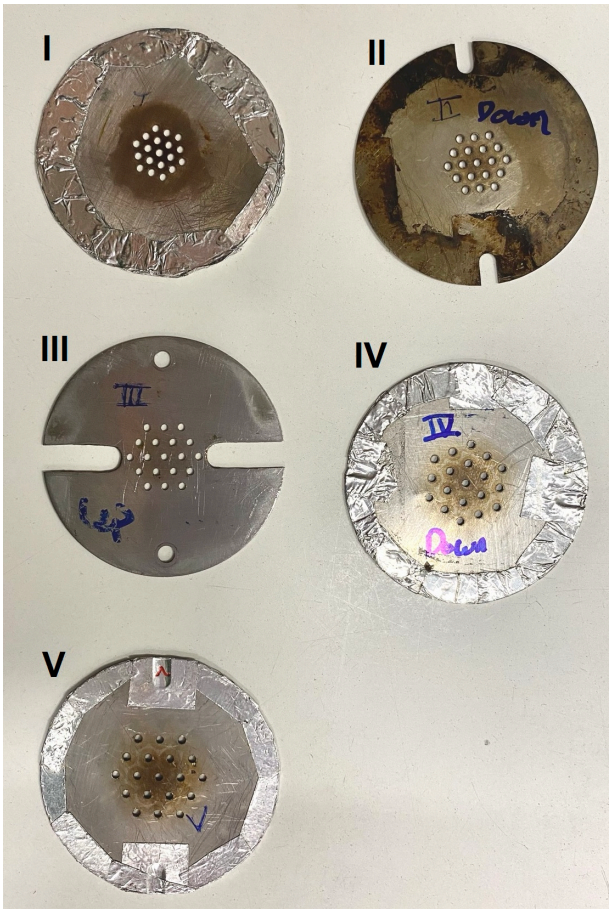

Figure 2.3: MPPs used in the experiments. Perforation ratio reduces from I to V.

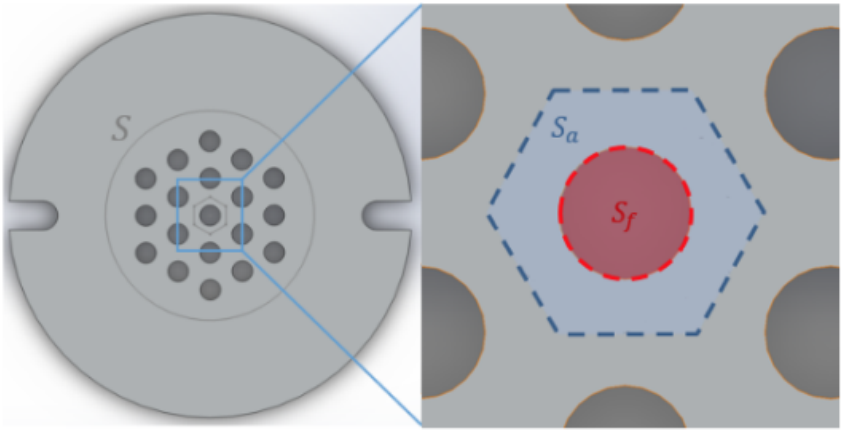

Figure 2.4: Schematics of the MPPs. Definition used for the perforation ratio parameter. [15]

Table 2.1: Geometrical parameters of the burner and plates.

Parameter	**Value**
Cavity Length (L)	60<L<450 mm
Cavity Internal Diameter (D)	43.5 mm
Plate hole diameter (d_h)	1.5 mm
Number of holes (n_h)	19
Porosity ($\mathcal{P}$)	2.3%
Plate thickness (l)	0.5 mm
Perforation Ratio (ψ)	
Plate I	35.5%
Plate II	26.9%
Plate III	20.5%
Plate IV	13.1%
Plate V	5.7%

2.1.3 Fuel Blends

The experiments were conducted with the mixture at atmospheric pressure and temperature, with *Re* from 60 to 275 and $0.5 \leq \phi \leq 1.8$. *Re* and ϕ are defined as follows:

$$Re = \frac{u\, d_h\, \rho}{\mu} \tag{2.2}$$

$$\phi = \frac{\text{AFR}_{st}}{\text{AFR}} = \frac{(n_{air}/n_{fuel})_{st}}{n_{air}/n_{fuel}} = \frac{(Q_{air}/Q_{fuel})_{st}}{Q_{air}/Q_{fuel}} \tag{2.3}$$

where u, ρ and μ are the mean mixture's velocity, mixture's density and mixture's dynamic viscosity respectively. AFR is the fuel-to-air ratio, the subscript st means the stoichiometric value of that property, n_i and Q_i is the molar quantity and is the absolute volumetric flow for the i fluid respectively. Q_{fuel} is defined by the sum of the volumetric flow rates of the fuels used for that experiment.

The fuel blends used were 100% C_3H_8, 100% CH_4 and 90% CH_4 + 10% H_2 in volume (v/v). Air was drawn from the atmosphere and compressed, filtered and desiccated. The fuel gases were provided in Alphagaz™ N35 research bottles from Air Liquide and have a purity of 99.95% (v/v). The mixture's μ was calculated through the Cantera toolbox in Python accompanied by the GRI-Mech 3.0 mechanism with the "Multi" transport model [30, 31]. The individual gas properties used can be found in table 2.2.

Table 2.2: Properties of the used gases.

Property	**Air**	**Methane**	**Hydrogen**	**Propane**
M [kg kmol^{-1}]	28.77	16.043	2.016	44.097
μ [Pa s$^{-1}\times 10^{-6}$]	18.48	11.389	8.961	8.174
ρ [kg m^{-3}]	1.176	0.656	0.0824	1.803

The flowrate of each gas and air were individually controlled by flowmeters. Alicat Scientific M series

mass flow meter of 5 standard litres per minute (SLPM) was used to regulate methane and propane, while another flowmeter of 50 SLPM was used for air and 1 SLPM for hydrogen. The uncertainty related to the set-point and the capacity of the air flowmeter is ± 0.8% and ± 0.2% respectively, with a total of $e_Q = 0.008\bar{Q} + 0.002Q_{max}$ ($\bar{Q}$ is the measured mean flow and Q_{max} is the flowmeter's maximum capacity). The remaining flowmeters have an uncertainty of the maximum between ± 0.6% set-point or ± 0.1% capacity.

The uncertainties of the flowmeters propagate to ϕ and total flow rate ($Q = Q_{air} + Q_{CH_4} + Q_{H_2}$ or $Q = Q_{air} + Q_{C_3H_8}$). Expressions for the uncertainties can be found using error propagation:

$$e_\phi^2 = e_{Q_{air}}^2 \left(\frac{\partial \phi}{\partial Q_{air}}\right)^2 + \sum_g e_{Q_g}^2 \left(\frac{\partial \phi}{\partial Q_g}\right)^2 \tag{2.4}$$

$$e_Q^2 = e_{Q_{air}}^2 \left(\frac{\partial Q}{\partial Q_{air}}\right)^2 + \sum_g e_{Q_g}^2 \left(\frac{\partial Q}{\partial Q_g}\right)^2 \tag{2.5}$$

where g is each fuel gas used for that mixture.

The maximum relative values of uncertainty for Q and ϕ are 8.97% and 21.87% respectively, however, these only appear for the extreme working conditions of *Re* $= 60$ and $\phi = 0.5$ using 100% C_3H_8 as fuel. At more commonly used working conditions such as *Re* $= 180$ and $\phi = 1.1$ the maximum relative uncertainty is 4.95%, which happens for ϕ using 100% C_3H_8 as fuel. Table 2.3 shows the uncertainties for the more common working conditions of *Re* $= 180$ and $\phi = 1.1$.

Table 2.3: Uncertainty values for all fuel blends. Working conditions of *Re* $= 180$ and $\phi = 1.1$.

Fuel Blend	Property	Absolute	Relative
100% CH_4	ϕ	0.0431	3.92%
	Q (SLPM)	0.1277	3.32%
90% CH_4 + 10% H_2	ϕ	0.0427	3.88%
	Q (SPLM)	0.1277	3.29%
100% C_3H_8	ϕ	0.0544	4.95%
	Q (SLPM)	0.1271	3.60%

2.2 Equipment and Data Acquisition

The data gathered for this thesis was obtained from a setup with microphone (see figure 2.5), acquisition board and high-speed camera (see figure 2.6). The equipment and setup are explained in the next paragraphs.

Pressure oscillations and frequency of the instabilities were measured using a Bruel Kjr – Type 4189 condenser microphone at a radial distance of 150 mm from the burner centre. The microphone has a linear response to frequencies in the range of 6.3 Hz up to 10 kHz, a distortion of smaller than 0.01% and a dynamic range from 14.6 dB to 146 dB. A BK 2250 pre-amplifier was used to boost the signal picked

from the microphone and the data was acquired by the Data Translation DT9841-VIB-SB acquisition board.

The data acquired by the data acquisition board was post-processed and the response of the thermoacoustics was obtained in the frequency domain through a Fast Fourier Transformation (FFT). The digitalization introduced in the Data Translation DT9841-VIB-SB board has an error of 0.3 mV in absolute amplitude, which represents less than 0.1% of its maximum, allowing us to neglect it when going through the procedures [32].

High-speed videos of the flame oscillations were recorded with a Phantom v4.2 camera with a capture rate of 5000 frames per second (fps) at 320$\times$240 pixels resolution and a capture rate of 9009 fps at 256$\times$192 pixels resolution. The images were tweaked and a false colour gradient was added to improve their visualisation. A full schematic of the experimental setup overview is shown in figure 2.7.

Figure 2.5: Microphone system used for capturing the frequencies and sound pressure level of the sound emitted by the instabilities.

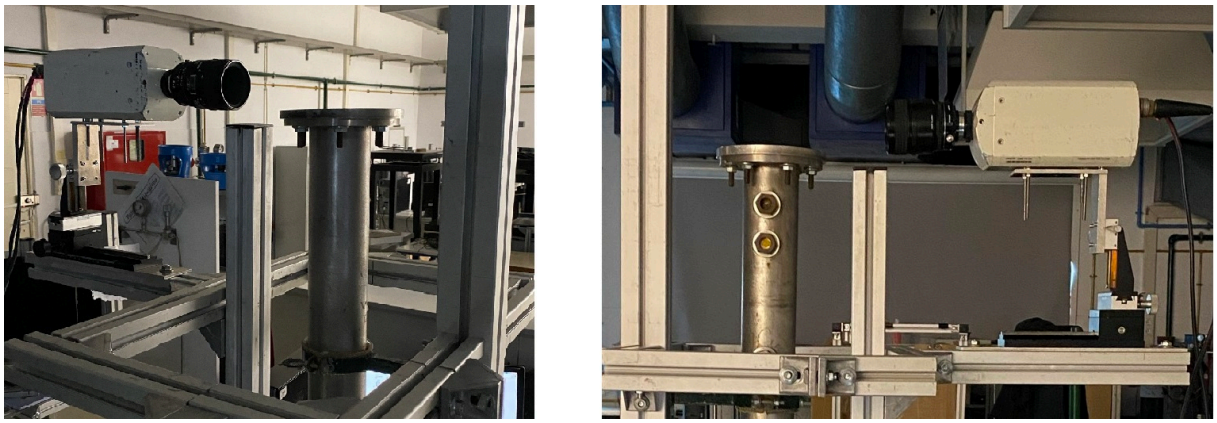

Figure 2.6: Burner setup with the high-speed camera.

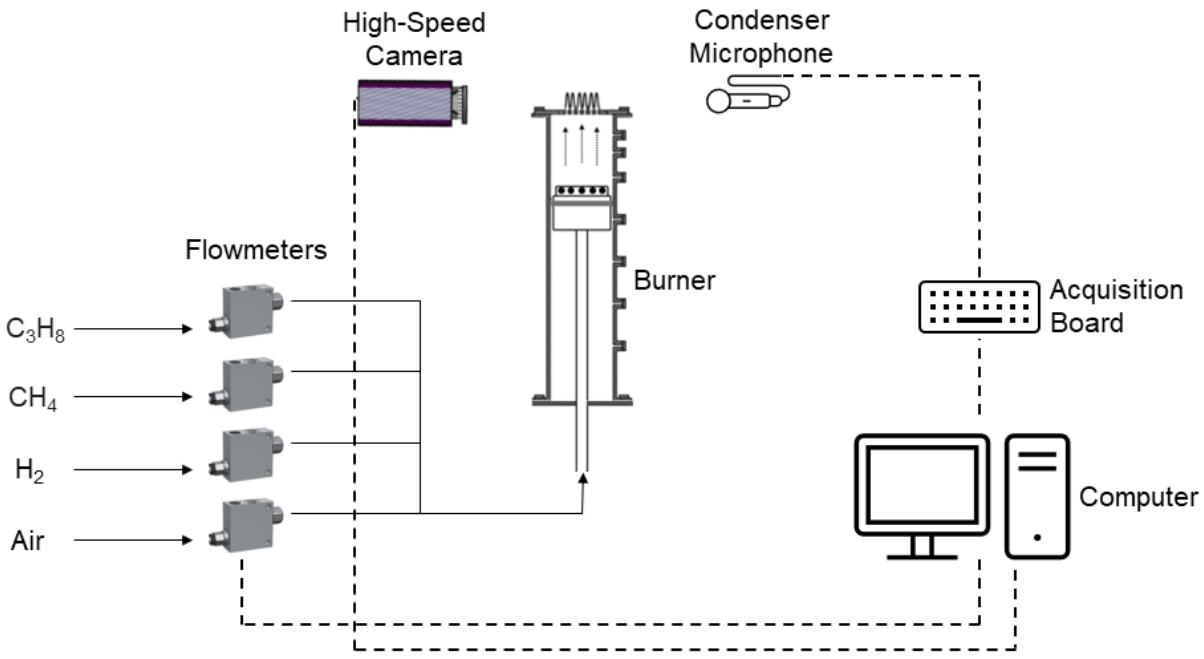

Figure 2.7: A schematic representation of the experimental setup. Solid lines are where the fuel flows and dashed lines are where data/information flows.

Chapter 3

Mathematical Models

A mathematical model for the resonating coupling phenomena between the burner acoustics and flame dynamics is presented in this chapter. This model has the objective to predict the thermoacoustic instabilities with respect to the burner geometry and fuel running conditions.

Firstly, an acoustic model of the burner without flames based on Tijdeman [33] is presented, where the acoustics depend on the mixture's properties such as the fuel composition and its incoming velocity. After that, a model for the flames energy release is shown. To close the model, an energy balance is made to predict the onset of thermoacoustic instabilities. A similar model was applied by Ferreira [15].

3.1 Burner Acoustic Model

For the acoustic model of the burner, it is considered that the tube cavity can be modelled as a perfect tube with one end closed by a wall and the other by a perforated thin plate. It was also assumed that only the longitudinal acoustic modes are relevant inside the tube, since the cavity length is larger than the its diameter ($L \gg D$).

Each acoustic flow variable is separated in two with the convention $a = \bar{a} + a'$, where $\bar{a}$ and a' are the mean and acoustic fluctuation respectively. The last component is often represented as $a' = \tilde{a}e^{i\omega t}$, with $\tilde{a}$ as the complex form of the perturbed variable and ω as the angular frequency ($\omega = 2\pi f$). The tube without a perforated plate is considered open ended and its specific acoustic impedance $z = p'/u'$, where p' and u' are the pressure and velocity fluctuation of the flow respectively, would disappear in the exhaust section. Through acoustics theory, the resonant frequencies of the open tube would be calculated with $\cos(\omega L/c) = 0$, for which the solution

$$f_n = \frac{(2n+1)\,c}{4L}, \text{with } n \in \mathbb{N}_0 \tag{3.1}$$

is valid, with c as the speed of sound. The solution to equation 3.1 with $n = 0$ is the first resonant mode, also known as the quarter wavelength resonator solution ($L = \lambda/4$).

With the perforated plate covering the end of the tube, a solution with the effects of the plate's impedance needs to be taken into account. For this, an analysis based on previous studies done by

Tijdeman [33] is presented here. The full steps of the original study can be found in Appendix B. It is possible to show that there are four parameters determining the solution of a propagating wave for tiny sinusoidal amplitudes of a flow inside a rigid tube:

$$\text{Shear wave number,} \qquad s = r\sqrt{\frac{\rho_s \omega}{\mu}} \tag{3.2}$$

$$\text{Reduced frequency number,} \qquad k = \frac{\omega r}{c} \tag{3.3}$$

$$\text{Square root of the Prandtl number,} \qquad \sigma = \sqrt{\frac{\mu C_P}{\kappa}} \tag{3.4}$$

$$\text{Specific heats ratio,} \qquad \gamma = \frac{C_P}{C_V} \tag{3.5}$$

If we consider the values of σ and γ constant, we end up with only the shear wave number (or Stokes number) and the reduced frequency number to work with. It is noteworthy that the Strouhal number *Sh*, which is not used for this model, can be important in wave propagation of oscillatory flows if the formation of vortices happens [34].

For $k \ll 1$ and $k/s \ll 1$, the solutions of the Low Reduced Frequency are valid [33]. In our case, the maximum frequency is around 750 Hz, which leads to a $k_{max} \approx 0.0033$ and $k/s \approx 1.13 \times 10^{-5}$, validating the solution for this work. The final solutions for pressure, axial velocity, density and temperature perturbations in the Low Reduced Frequency are:

$$\tilde{p} = A_1 e^{\Gamma\xi} + B_1 e^{-\Gamma\xi} \tag{3.6}$$

$$\tilde{u} = \frac{i\Gamma}{\gamma}\left[1 - \frac{J_0(i^{3/2}\eta s)}{J_0(i^{3/2}s)}\right]\left(A_1 e^{\Gamma\xi} - B_1 e^{-\Gamma\xi}\right) \tag{3.7}$$

$$\tilde{\rho} = \left[1 - \frac{\gamma - 1}{\gamma}\left(1 - \frac{J_0(i^{3/2}\sigma\eta s)}{J_0(i^{3/2}\sigma s)}\right)\right]\left(A_1 e^{\Gamma\xi} + B_1 e^{-\Gamma\xi}\right) \tag{3.8}$$

$$\tilde{T} = \frac{\gamma - 1}{\gamma}\left[1 - \frac{J_0(i^{3/2}\sigma\eta s)}{J_0(i^{3/2}\sigma s)}\right]\left(A_1 e^{\Gamma\xi} + B_1 e^{-\Gamma\xi}\right) \tag{3.9}$$

where η is the radial non-dimensional coordinate ($\eta = r/R$), ξ is the axial non-dimensional coordinate ($\xi = x/L$) and Γ is defined as:

$$\begin{aligned} \Gamma &= \frac{J_0(i^{3/2}s)}{J_2(i^{3/2}s)}\sqrt{\frac{\gamma}{n}} \\ \text{with, } n &= \left[1 + \frac{\gamma - 1}{\gamma}\frac{J_2(i^{3/2}\sigma s)}{J_0(i^{3/2}\sigma s)}\right]^{-1} \end{aligned} \tag{3.10}$$

The values of constants A_1 and B_1 are determined by defining additional boundary conditions at both ends of the tube, J_0 and J_2 are the Bessel functions of the first kind for integers 0 and 2 respectively. Although the heat transfer from the perforated plate to the feeding flow may contradict the pressure gradient imposed to the holes, it can be neglected since the thermal acoustic boundary layer (0.2 mm) is small compared to each hole's diameter (1.5 mm) [15]. Therefore, the equations 3.8 and 3.9 can be ignored.

With the equations presented so far, the specific acoustic impedance of the open tube (without the plate) can be treated as:

$$z_{tube} = \rho c \frac{\tilde{p}}{\tilde{u} \cdot \boldsymbol{n_b}} = \rho c \frac{A_1 e^{\Gamma\xi} + B_1 e^{-\Gamma\xi}}{\frac{i\Gamma}{\gamma}\left[1 - \frac{J_0(i^{3/2}\eta s)}{J_0(i^{3/2}s)}\right](A_1 e^{\Gamma\xi} - B_1 e^{-\Gamma\xi})} \tag{3.11}$$

The next step is adding the plate's impedance. For this, it is assumed that the burner can be modelled as a large tube and the perforated plate can be modelled as multiple small tubes with a length equal to the plate thickness, leading to a total burner impedance $z_{burner} = z_{tube} + z_{plate}$. The impedance defined by equation 3.11 has two unknowns in $A1$ and $B1$, meaning that the total burner impedance expression has four unknowns (two for the tube and two for the plate). Therefore, four boundary conditions must be applied to the model.

The chosen boundary conditions for the calculations are the following:

1. At the piston surface $x = 0$, the axial velocity is zero since it is a closed end;
2. At the boundary between the tube and plate $x = L$, the pressure is continuous between tube and holes inlet;
3. Still at $x = L$, there is mass flow conservation;
4. At the plate's exit $x = L + l$, the pressure meets the external conditions.

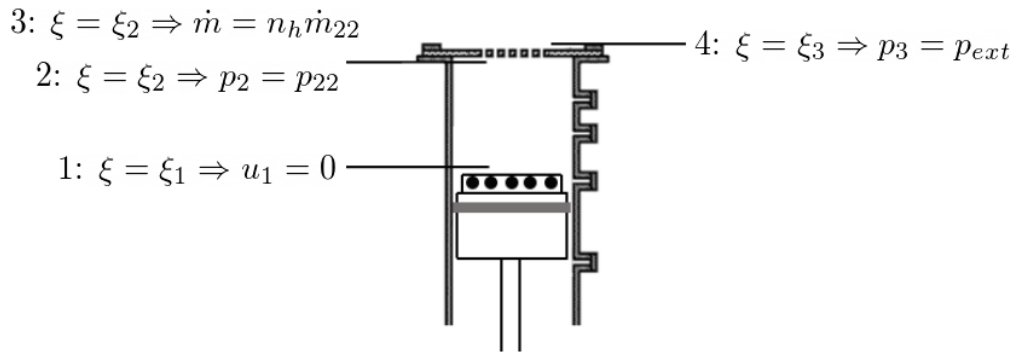

Figure 3.1: Boundary conditions applied to the burner for the mathematical model.

Following the convention adopted in figure 3.1, the mathematical formulations of them are:

$$1: \quad \frac{i\Gamma_1}{\gamma}\left[1 - \frac{J_0(i^{3/2}\eta s)}{J_0(i^{3/2}s)}\right]\left(A_1 e^{\Gamma_1\xi_1} - B_1 e^{-\Gamma_1\xi_1}\right) e^{i\omega t} = 0 \tag{3.12}$$

$$2: \quad A_1 e^{\Gamma_1\xi_2} + B_1 e^{-\Gamma_1\xi_2} = C_1 e^{\Gamma_2\xi_2} + D_1 e^{-\Gamma_2\xi_2} \tag{3.13}$$

$$3: \quad \int_0^{2\pi}\int_0^{R} u_2 r\, dr d\theta = n_h \int_0^{2\pi}\int_0^{r_h} u_{22} r\, dr d\theta \tag{3.14}$$

$$4: \quad p_3 = p_s\left[1 + \left(C_1 e^{\Gamma_2\xi_3} + D_1 e^{-\Gamma_2\xi_3}\right) e^{i\omega t}\right] \tag{3.15}$$

The total burner impedance is almost complete, since the parameters $A1$, $B1$, $C1$ and $D1$ are known with equations 3.12 to 3.15. The only remaining parameter to introduce is the perforation ratio ψ that was first referred to in chapter 2.1. Following Maa [16], the complete burner impedance is:

$$z_{burner} = z_{tube} + z_{plate} = \frac{\tilde{p}_2}{\tilde{u}_2 \cdot \boldsymbol{n_b}} + \left(\frac{\tilde{p}_3 - \tilde{p}_2}{\tilde{u}_3 \cdot \boldsymbol{n_b}}\right)\frac{1}{\psi} \tag{3.16}$$

The definition of ψ is given by equation 2.1 and it relates to the separation between perforations, opposing to porosity $\mathcal{P}$ which relates to the ratio of perforated and non-perforated area. In this work, the porosity of the different plates is maintained constant at $\mathcal{P} = 2.3\%$.

This mathematical model for the burner acoustics was validated using plate I. Through figure 3.2 it is possible to observe that the assumption of only longitudinal waves through the tube is capable of modelling the burner acoustics [15].

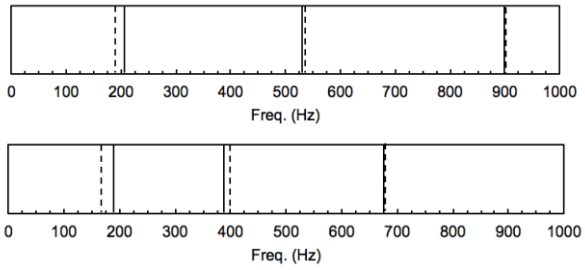

Figure 3.2: Experimental (solid lines) and mathematical model (dashed lines) results for the resonant modes of the burner with plate I done by Ferreira [15]. Bottom: $L = 57$cm. Top: $L = 42$cm.

Additionally the effect of viscous dissipation in the model was verified. At a first glance, the resonant modes of the complete burner should be the same as the tube alone however, analysing equations 3.6 and 3.7 it is possible to see that these depend on the plate's parameters (l, L and d_h). Figure 3.3 shows the theoretical resonant frequencies of the burner through L for the burner with and without plate. The solutions for the tube alone (cos$(\omega L/c) = 0$) differ from the solutions with the plate's effects considered.

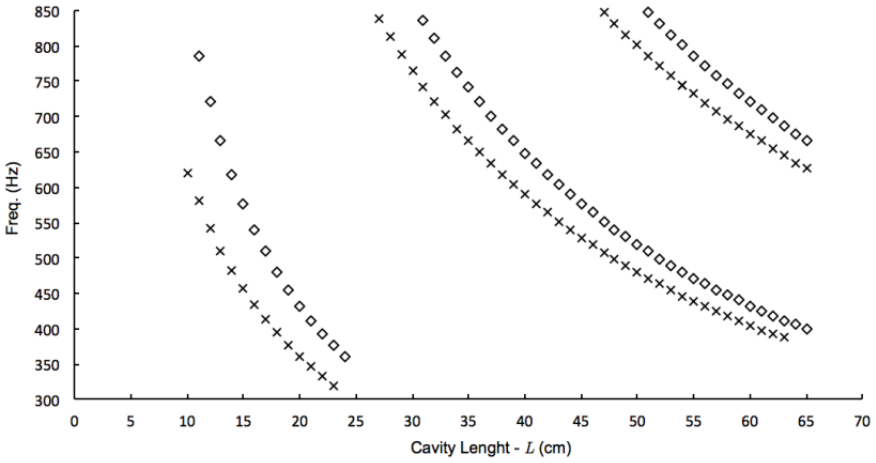

Figure 3.3: Results for resonance frequencies as function of the cavity's length from [15]. ($\times$) Symbol represents the solution with plate's effects. ($\diamond$) Symbol represents the non viscous effects solution.

3.2 Flame Model

As we can recall from equation 1.2, to have resonance it is required that the externally applied forces overcome the dissipative ones. For that it is necessary to express the acoustic velocity fluctuations with respect to pressure fluctuations at the exhaust section. The heat release rate fluctuations generate a pressure fluctuation at the same frequency, meaning that the pressure fluctuation is proportional to the heat release rate fluctuation:

$$p' \propto \left[\frac{\partial q'}{\partial t}\right]_{t-\tau_{ac}} \tag{3.17}$$

where τ_{ac} is the acoustic propagation delay, corresponding to the time delay that the pressure wave generated at the tip of the flame reaches the burner's exit.

It is possible to use the flame surface area as a parameter to compute the heat release since the flame surface is roughly proportional to the heat release rate [13], leading to the following definition for the pressure fluctuation:

$$p' = \frac{\rho_\infty}{4\pi H}\left(\frac{\rho_u}{\rho_b} - 1\right) S_L \left[\frac{\partial A'}{\partial t}\right]_{t-\tau_{ac}} \tag{3.18}$$

where ρ_∞ is the volumetric weight of the surrounding air, ρ_u and ρ_b are the unburned and burned gases volumetric weight respectively, H is the distance from the tip of the flame to the burner's exit (which is the flame height H_f), A' is the flame surface area fluctuation and S_L is the laminar flame speed of the mixture. If there is formation of vortices, then turbulent flame speed should be considered [35].

The values for ρ_u/ρ_b were calculated for different equivalence ratios ϕ using the Cantera toolbox in Python with the GRI-Mech 3.0 mechanism [30, 31]. Flame speed for both mixtures (100% CH_4 and 90% CH_4 + 10% H_2) used in this thesis were based on Quintino and Fernandes [36] correlations, with the base CH_4 flame speed from Coppens *et al.* [37] (see figure 3.4).

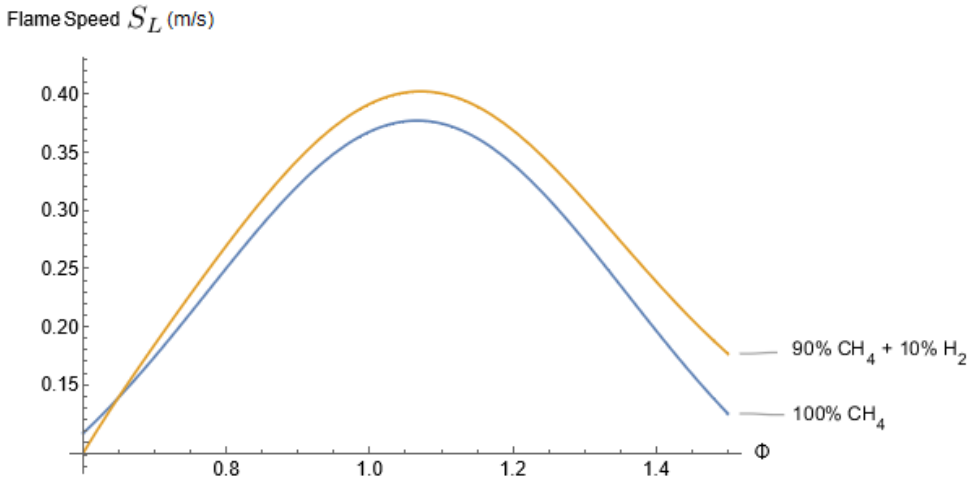

Figure 3.4: Flame speed S_L with respect to ϕ for both mixtures studied in the model.

To evaluate the heat release in an analytical formula, the Flame Transfer Function (FTF) method is used. The FTF is used to characterise the flame response to the imposed velocity oscillations through a

transfer function, as one can recall from equation 1.4:

$$FTF(\omega) = \frac{q'/\bar{q}}{u'/\bar{u}} = G_\omega e^{i\omega\tau_{cv}} \tag{3.19}$$

where the expression on the right is a more classical representation of transfer functions in the frequency domain. Here G_ω is the function's gain and τ_{cv} is the convective time delay, which is the time that perturbation from the burner's exit takes to the flame's tip. An experimentally obtained FTF for the burner configuration used in this work was achieved by Leitão [38] through simultaneously recording the light emitted by the flames and the velocity perturbations in forced flow experiments. The gain and phase of the FTF are:

$$G_\omega = \left| \frac{0.96}{1 - 1.258i\,(\omega/2999) - (\omega/2999)^2} \right| \tag{3.20}$$

$$\varphi = \frac{2.33\pi}{1000} f \tag{3.21}$$

Figure 3.5 shows that the transfer function has a behaviour similar to that of a low-pass filter and the phase linearly scales with frequency.

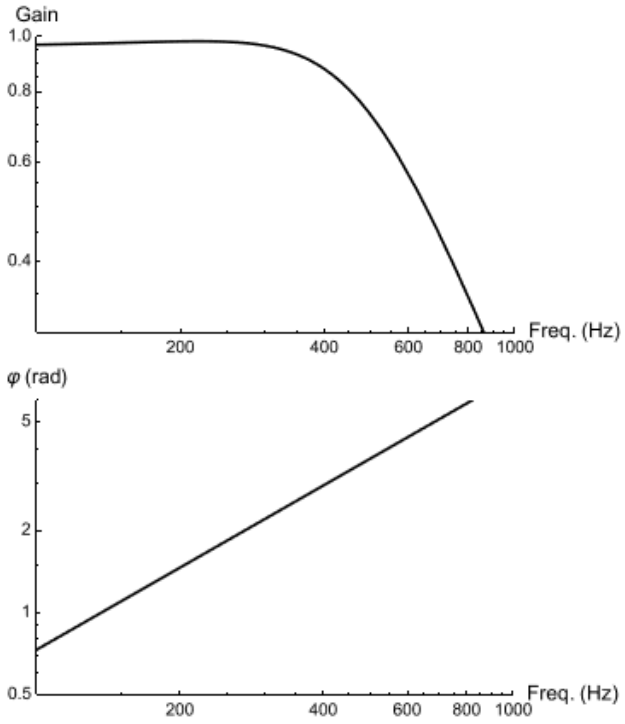

Figure 3.5: FTF gain and phase from the measurements performed by Leitão [38].

Through equations 3.18 and 3.19 and considering the proportionality of the flame heat release with the flame surface area we obtain:

$$p' = \frac{\rho_\infty}{4\pi H}\left(\frac{\rho_u}{\rho_b} - 1\right) S_L G_\omega \frac{\bar{A}}{\bar{u}} \left[\frac{\partial u'}{\partial t}\right]_{t-\tau} \tag{3.22}$$

Considering the complex form of the velocity and pressure fluctuation:

$$\begin{aligned}\tilde{p}e^{i\omega t} &= \frac{\rho_\infty}{4\pi H}\left(\frac{\rho_u}{\rho_b}-1\right)S_L G_\omega \frac{\bar{A}}{\bar{u}}\left[\frac{\partial}{\partial t}\left(\tilde{u}e^{i\omega(t-\tau)}\right)\right] \Leftrightarrow \\ \tilde{p}e^{i\omega t} &= \frac{\rho_\infty}{4\pi H}\left(\frac{\rho_u}{\rho_b}-1\right)S_L G_\omega \frac{\bar{A}}{\bar{u}}\tilde{u}e^{-i\omega\tau}e^{i\omega t}\end{aligned} \tag{3.23}$$

with τ as the total time delay, composed from the acoustic and convective time delays $\tau = \tau_{ac} + \tau_{cv}$. With the results from equation 3.23 and the definition of impedance, it is possible to obtain the flame impedance equation that connects pressure and velocity fluctuations:

$$z_{flame} = \frac{\tilde{p}}{\tilde{u}\cdot \boldsymbol{n_f}} = -i\omega\frac{\rho_\infty}{4\pi H}\left(\frac{\rho_u}{\rho_b}-1\right)S_L G_\omega \frac{\bar{A}}{\bar{u}}e^{i\omega t} \tag{3.24}$$

Both, flame and burner impedance will be used to compute the driving forces and compare their power to the dissipative ones in an energy balance around the power exchange surface (see figure 3.6).

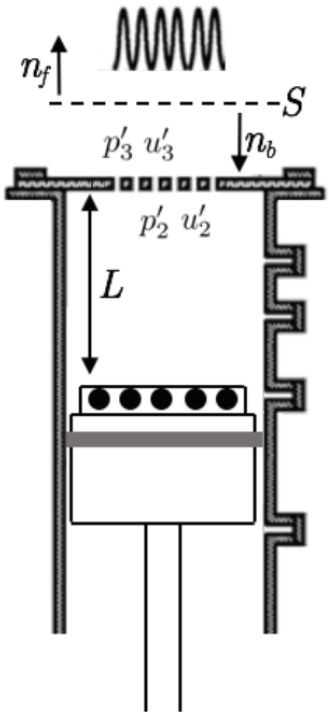

Figure 3.6: Representation of the burner with flames and the power exchange surface (S).

3.3 Energy Balance

Recalling the formulation given by Zinn [11] in equation 1.2 it is possible to interpret the requirement for self-sustained oscillations as the existence of a driving power P_{driv} superior to the dissipative power P_{diss}:

$$|P_{driv} > P_{diss}| \tag{3.25}$$

This energy balance can be calculated in the surface S shown in figure 3.6, while the acoustic power

is computed by averaging over a period of oscillation T, such that:

$$P = \int_S \frac{1}{T} \int_0^T \Re(p')\Re(u' \cdot \boldsymbol{n}),\, dtdS \tag{3.26}$$

where $\Re(a)$ is the real part of a. Equation 3.26 over the surface S as a harmonic perturbation leads to:

$$P = \frac{S}{2}\Re(\tilde{p}\tilde{u} \cdot \boldsymbol{n}) = \frac{S}{2}\Re(z)\,|\tilde{u}|^2 \tag{3.27}$$

Therefore, the condition of equation 3.25 becomes:

$$\frac{S}{2}\,|\Re(z_{flame})|\;|\tilde{u}|^2 > \frac{S}{2}\Re(z_{burner})\;|\tilde{u}|^2 \tag{3.28}$$

Using the definitions of z_{flame} and z_{burner} given by equations 3.24 and 3.16 respectively, it is possible to determine which frequencies can lead to resonance given the working conditions of the burner, *i.e.* knowing the fuel mixture and velocity, cavity length and plate it is possible to determine if a given frequency leads to self-sustained sound generation.

It is also important to note that in equation 3.28 the flame impedance factor comes as an absolute value, meaning that $\Re(z_{flame})$ can be negative and still help to produce sound. This is because the acoustic energy generated by self-sustained oscillations from combustion can be directed towards the burner, which through the convention in figure 3.6 means a negative value, and still enhance the production of sound [12]. This condition happens when the harmonic form of the driving power takes the values of $\sin(\omega\tau) < 0$, which is when $\omega\tau \in]n\pi, (n+1)\pi[$ where $n = \{2k+1 \,:\, k \in \mathbb{N}_0\}$.

Chapter 4

Results

This chapter has the demonstration and analysis of the experimental results and mathematical model's performance. First an analysis of the LBO limits and flame stability is shown to understand the influence of fuel and plates on the flammability range of the burner and the onset of thermoacoustic instabilities. After that, evaluation of the frequencies and sound pressure level for the instabilities is made. Then, discussion of the flame shape through the instabilities is presented with support from the high-speed camera images. To finalise, results of frequency with respect to the cavity length L are shown and discussed accompanied by an evaluation of the mathematical model.

4.1 LBO Limits and Stability Maps

4.1.1 Lean-blowout Limits

Results for all plates show a significant higher ϕ for C_3H_8 limits, even spanning rich values ($\phi > 1$) for *Re* above 200 in plate III, *Re* above 125 in plate IV and even *Re* below 100 in plate V. The line shown for each graph in figure 4.1 represents the LBO limit, *i.e.* when the flame cannot be sustained and extinguishes. The region at the left of the line indicates when the flame cannot burn and at the right when flames can be self-sustained.

The CH_4 fuel allows a significant extension of the LBO limit, leading to a reduction up to around 0.3 in ϕ at $Re = 260$, show in plates IV and V at $Re = 260$. Additionally, although the fraction of H_2 was only 10%, its influence is already noticeable. A relevant extension of the LBO limit is seen when compared to the pure CH_4 blend, suggestion that with higher H_2 fractions the limits can be further extended and leaner applications may be used without changing the burner's geometry. This is in agreement with studies found in [23, 28], even though those experiments were done at higher *Re*, up to 19000.

Separation between holes is also an important factor to consider when evaluating LBO limits. Even though, plates I and II do not have a very noticeable difference between their limits, the results for other plates show otherwise. A lower ψ leads to a decrease of the limits, even pushing the 100% CH_4 and 90% CH_4 + 10% H_2 blends to richer values in plate V. This is expected since the small flames from each hole have less possibility to sustain each other as they get further apart. It is curious to note that although

plate II has a lower ψ, the limit is slightly extended for the 100% CH_4 and 90% CH_4 + 10% H_2 mixtures when compared to plate I.

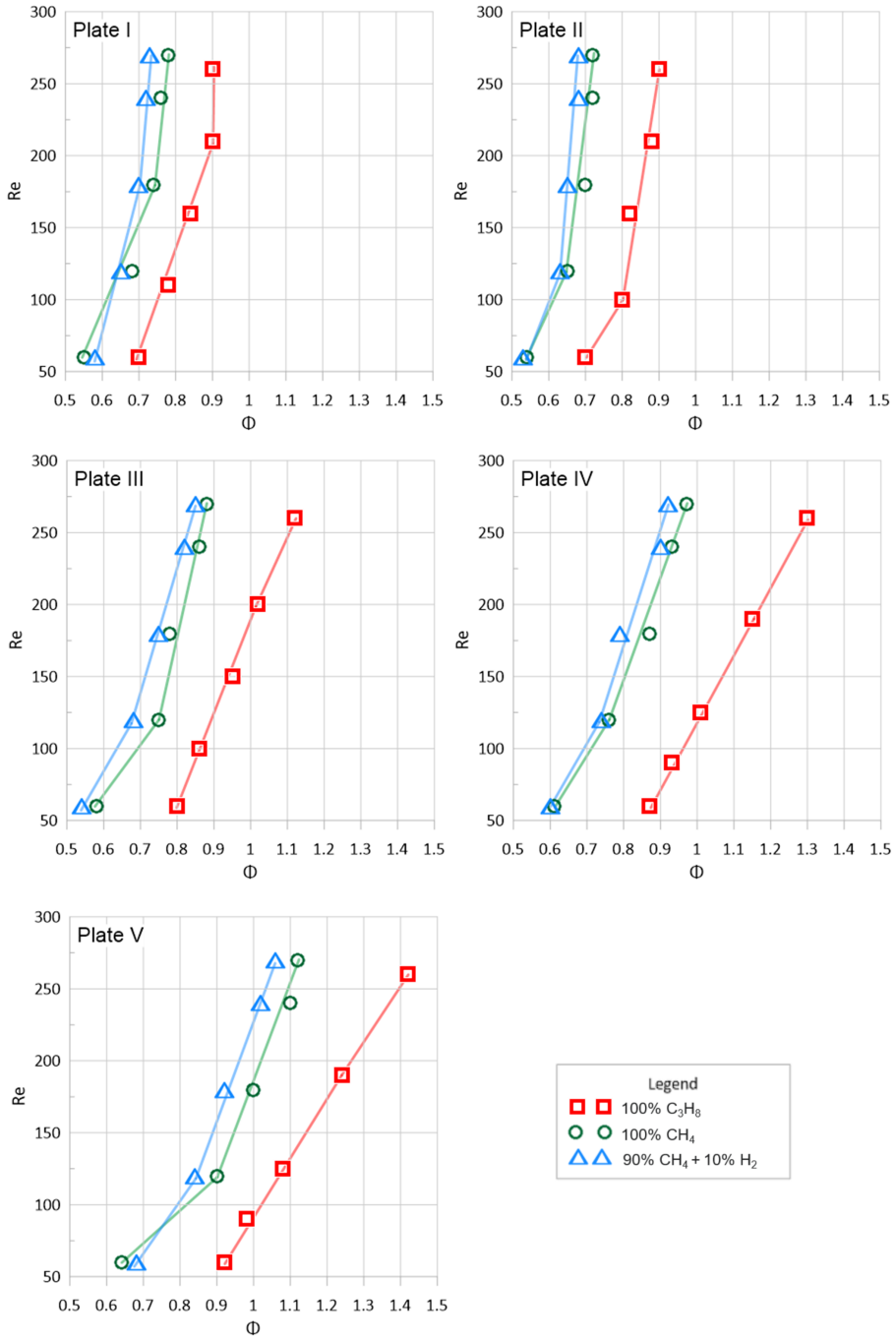

Figure 4.1: Lean blow-off limits for the different plates and fuels at $L = 12$ cm.

4.1.2 Flame Stability

To further study the relevancy of different fuel blends and plates, an analysis of stability maps is made (see figure 4.2). These show where thermoacoustic instabilities occur in each plate with respect to the working conditions *Re* and ϕ.

C_3H_8 noise regions are larger for all plates when compared to the other fuel blends studied in this work, and in particular, plate V does not manifest a noise region for both 100% CH_4 and 90% CH_4 + 10% H_2. For plate I, C_3H_8 has the unstable region starting right after the LBO limit for *Re* above 125, meaning that as soon as flames can be sustained noise starts to appear.

The results for CH_4 show a clear reduction of the noise region when compared to C_3H_8, leading to a wider range of values for which the burner can run with no thermoacoustic instabilities. Yet, similar to the case for propane's plate I map, the margin between the LBO limit and noise region in plate I is very small, not allowing lean working conditions of the burner without generation of noise. Even though the plates III and IV have the smaller noise regions, the particular case of plate II with the tested conditions shows an increase in noise region when compared to plate I, which has the highest ψ.

Lean conditions with no thermoacoustic instabilities are found in plate I with the addition of H_2. This is due to the combination of a leaner LBO limit and the noise region shifting to richer values. No relevant size difference was found for the noise regions of plates I and II between 100% CH_4 and 90% CH_4 + 10% H_2, but a significant increase exists for plates III and IV. This suggests that an increase use of hydrogen in fuel mixture can lead to even wider undesired noise limits, since a presence of only 10% H_2 in volume has led to such expressive results.

Although a decrease in separation ratio (ψ diminishes with the plate numbers) indicates a smaller unstable region, its effects on the LBO limits cannot be ignored. It is important to reduce the possibilities of having thermoacoustic instabilities, but the objective of using leaner mixture for combustion applications needs to be complied. This means that through the results found and shown in figures 4.1 and 4.2 it is important to choose geometries with a balance between LBO limits and noise regions in mind, knowing that H_2 can also be an option to improve working conditions.

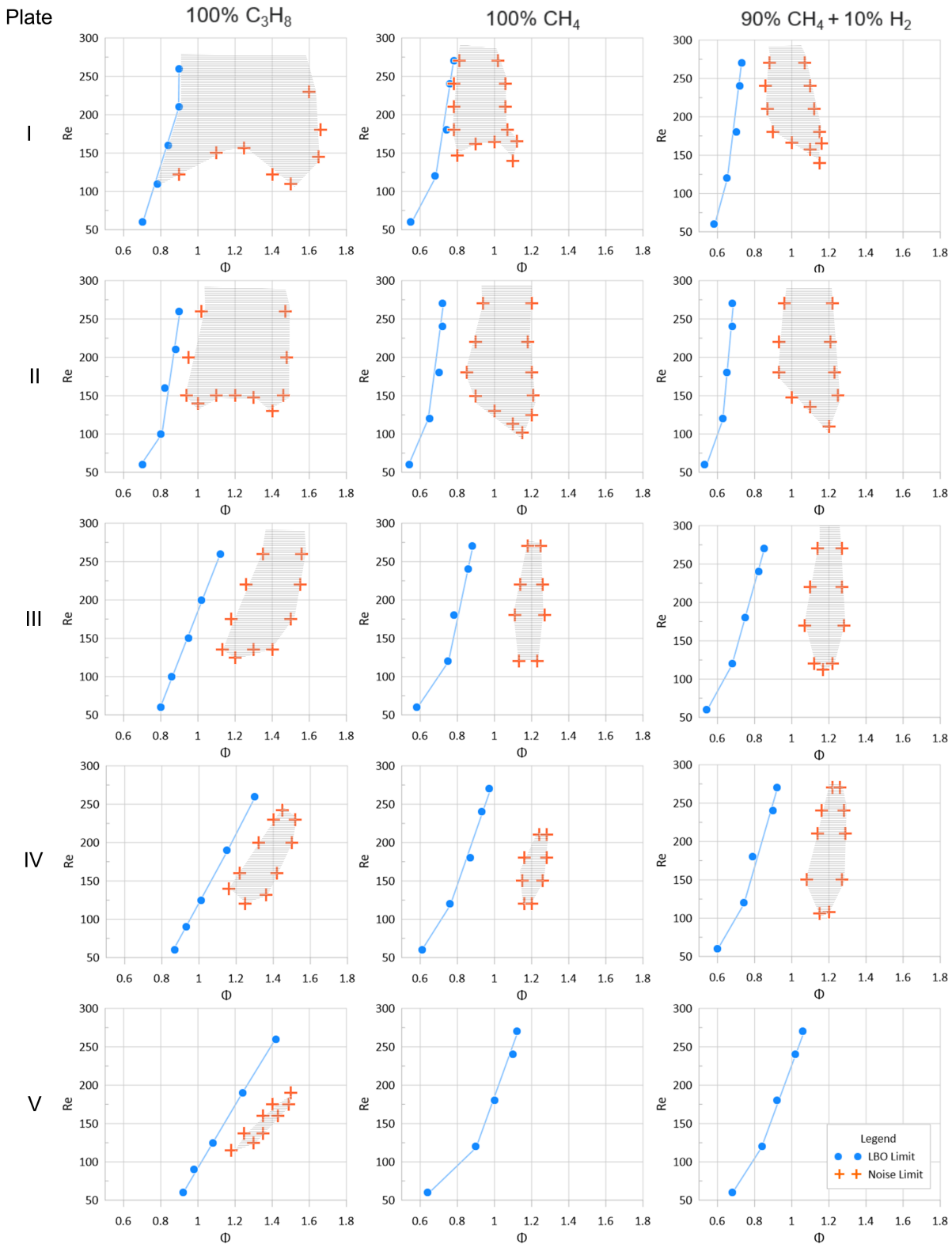

Figure 4.2: Stability maps for all plates and fuels studied at $L = 12$ cm. Shaded sectors represent the thermoacoustically unstable regions.

4.2 Frequency and Sound Pressure Level in Noise Regions

With the results from chapter 4.1 a further analysis on the thermoacoustic instabilities is made. Evaluation of the sound pressure level (SPL) and frequencies of the noise generated shown for 100% CH_4 and 90% CH_4 + 10% H_2 fuel blends for plates I to IV is done, since these two blends showed a clear advantage over C_3H_8 in LBO limits and thermoacoustic instabilities. Plate V was not evaluated because it did not show a noise region in the stability maps for 100% CH_4 and 90% CH_4 + 10% H_2 at $L = 12$ cm. One fixed *Re* and two fixed ϕ were chosen for each map.

For plate I with both fuel blends (see figure 4.3 and 4.4), even though the noise limits shifted to higher ϕ with the addition of H_2 seen from previous results, a slight peak of SPL exist at around $\phi = 1$ for both fixed *Re* studied of 220 and 180. This is a common factor with results shown by Ferreira [15], as it was also demonstrated that SPL had a slight peak at $\phi = 1$ for plate I but using C_3H_8. At a fixed $\phi = 0.9$, SPL has a tendency to drop at higher *Re*. Additionally, overall frequency results are higher for the H_2 enhanced fuel blend when compared to the pure CH_4 one.

The SPL with respect to ϕ has a different behaviour for plate II when compared to plate I. Instead of a slight peak at $\phi = 1$, SPL continues to rise as ϕ goes higher (see figures 4.5 and 4.6). More noticeable, the frequency has a significant decrease with respect to ϕ for both fuel blends. This drop is found for values of $\phi > 1$. It is a result not found for other plates, demonstrating an uniqueness of plate II. When ϕ is fixed, a disparity between both fuels exists, as 100% CH_4 results in a monotonous behaviour of SPL and frequency while 90% CH_4 + 10% H_2 demonstrates a drop of frequency and rise in SPL for higher *Re*. Plus, like in plate I, the instabilities for 90% CH_4 + 10% H_2 fuel blend are higher.

Frequency for both fuel blends does not change significantly with respect to ϕ and *Re* for plates III and IV (figures 4.7 to 4.10). The only significant difference is the SPL increase of plate III at higher *Re* while fixing ϕ at a constant value. SPL has a peak for plate IV with 90% CH_4 + 10% H_2, but it is inconclusive to the overall results. Similar to the previous mentioned plates, the addition of H_2 leads to higher frequencies when compared to 100% CH_4.

It is also important to note that the similar SPL for the same plate, but different fuel blends can be explained because SPL is a manifestation of the energy released by the flame. Taking into account the formulation in equation 3.28, the excess energy from the flame after overtaking the burner's damping processes is manifested in the oscillations amplitudes, which is the SPL. Since the mixture only has 10% H_2 the lower heating value (LHV) of the mixture does not change significantly, as $\text{LHV}_{100\%CH_4} = 50.02\,\text{MJ/kg}$ and $\text{LHV}_{90\%CH_4+10\%H_2} = 50.98\,\text{MJ/kg}$, which for working conditions of $\phi = 1$ and $Re = 200$ considering perfect combustion, for example, leads to heat release rates of $q_{100\%CH_4} = 0.2114\,\text{kJ/s}$ and $q_{90\%CH_4+10\%H_2} = 0.2156\,\text{kJ/s}$. This is a relative difference of only 1.9% with respect to the 100% CH_4 blend.

The overall results show that the presence of H_2 in the mixture leads to an increase in frequency values for all plates, this is in agreement with results of Kim *et al.* [29] where a shift to higher modes of resonance (higher frequencies) was correlated to a higher fraction of H_2 in the fuel composition, a consequence from the time delay reduction of the flame perturbation. Plate II shows a particular behaviour

for frequency not found in other plates, where there is a significant drop of frequency for $\phi > 1$ at fixed *Re*. Analysing the results with respect to the plates there are no significant correlations between them, suggesting that the main dependency of SPL and frequency with respect to ϕ and *Re* is on the plate itself, keeping in mind that H_2 fractions studied were not enough to influence significantly the heat release rate of the flame and therefore SPL.

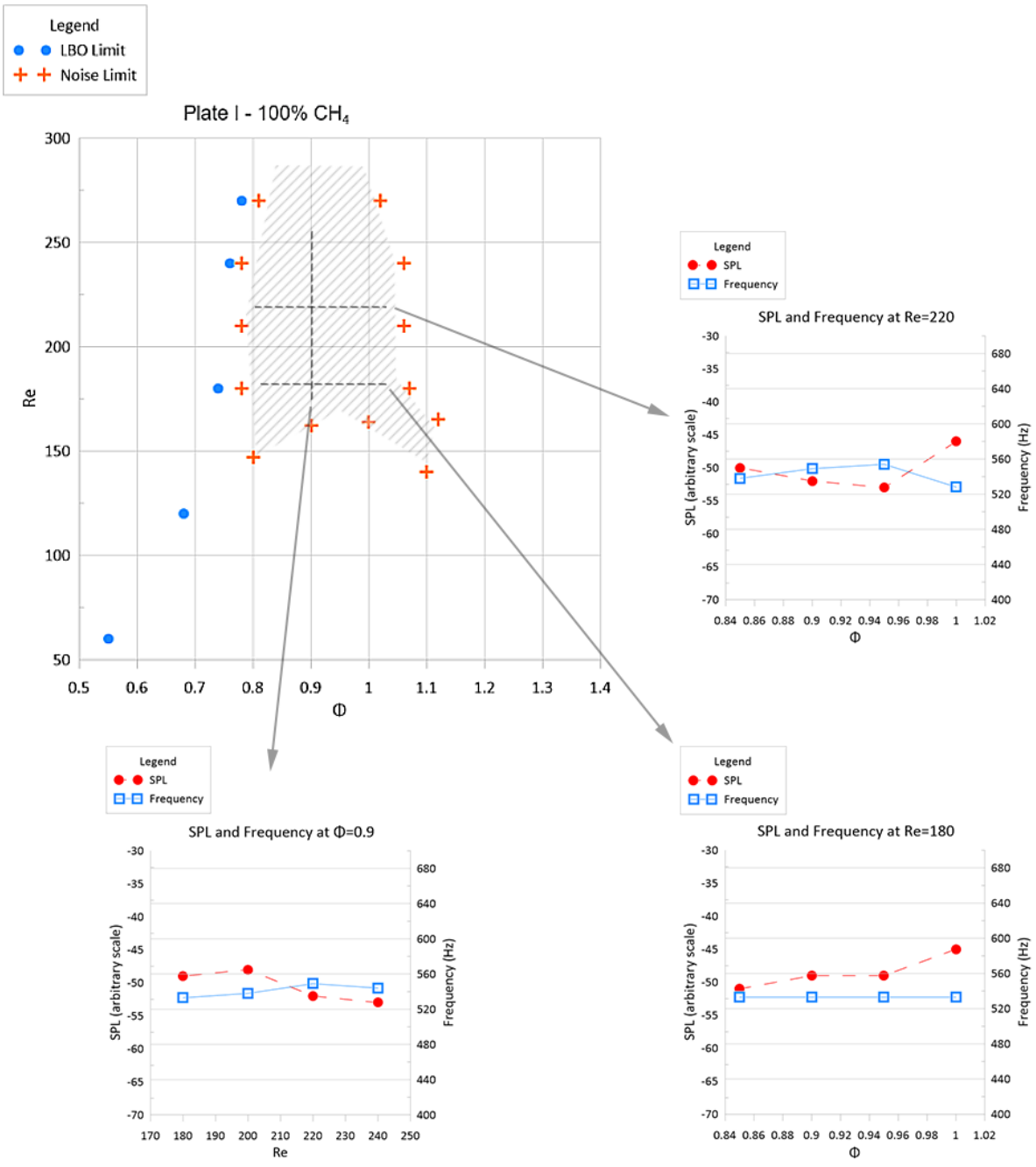

Figure 4.3: Plate I 100% CH_4 stability map at $L = 12$ cm with frequency and sound pressure level analysis for selected ϕ and Re.

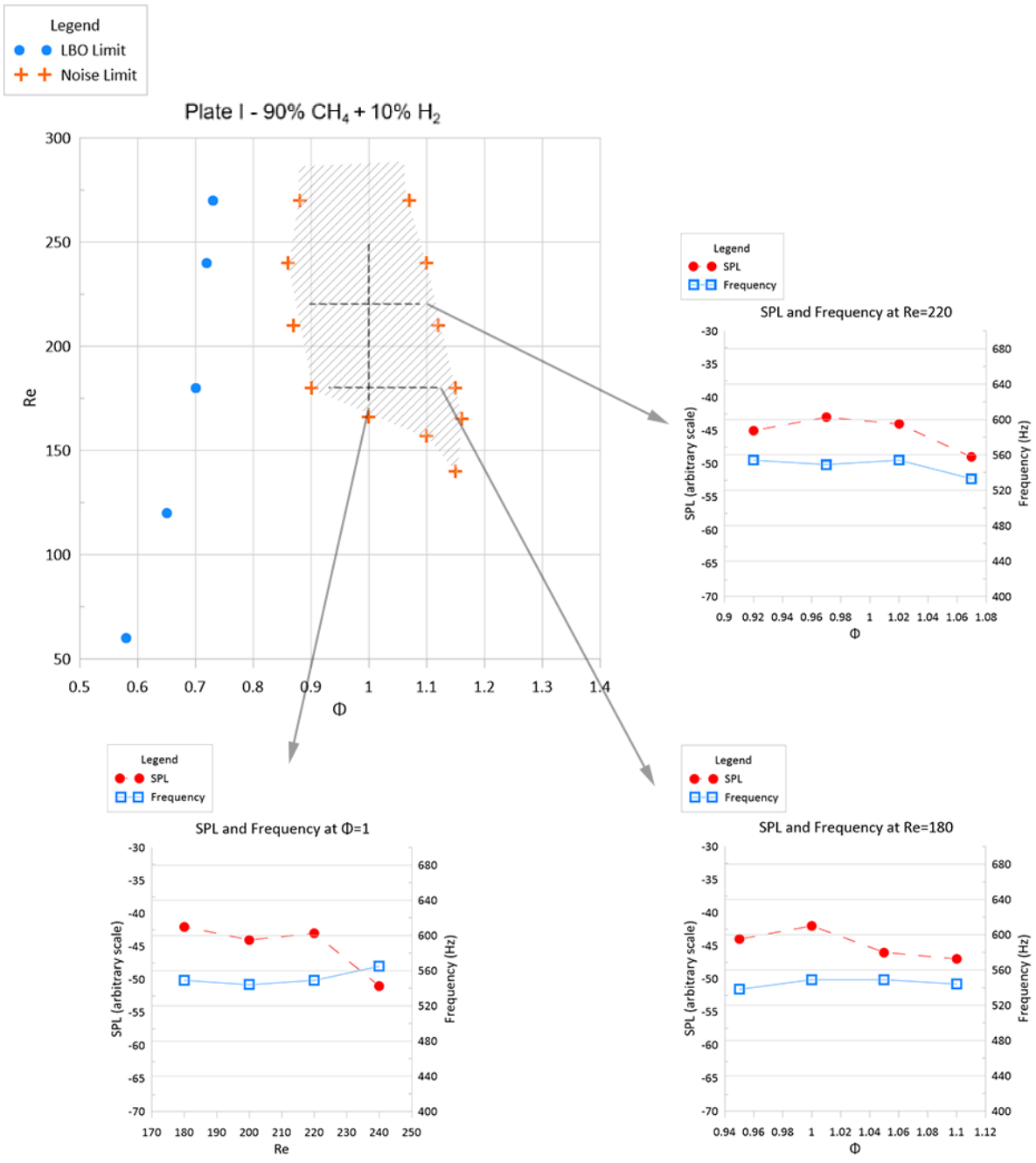

Figure 4.4: Plate I 90% CH_4 + 10% H_2 stability map at $L = 12$ cm with frequency and sound pressure level analysis for selected ϕ and Re.

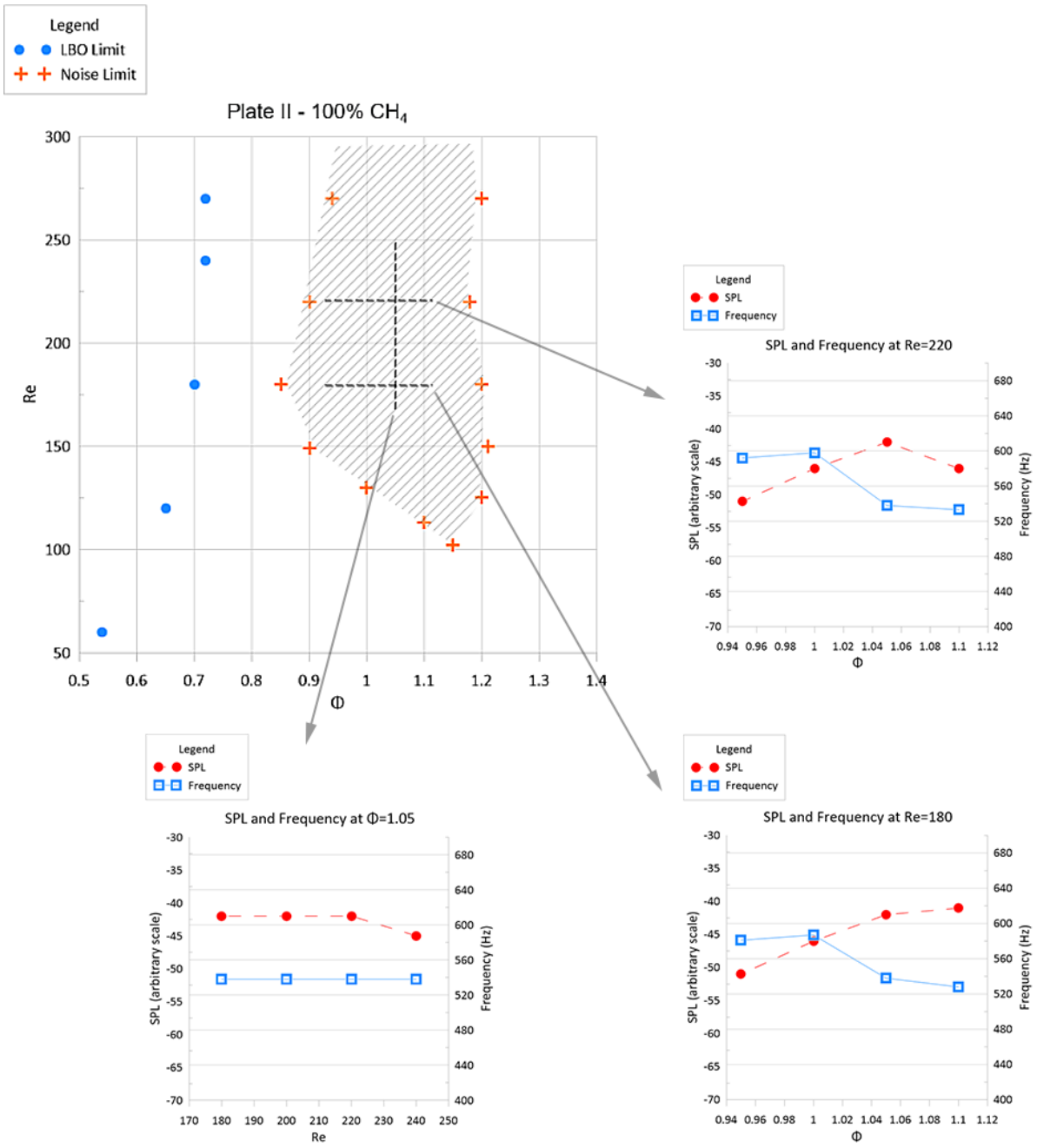

Figure 4.5: Plate II 100% CH_4 stability map at $L = 12$ cm with frequency and sound pressure level analysis for selected ϕ and Re.

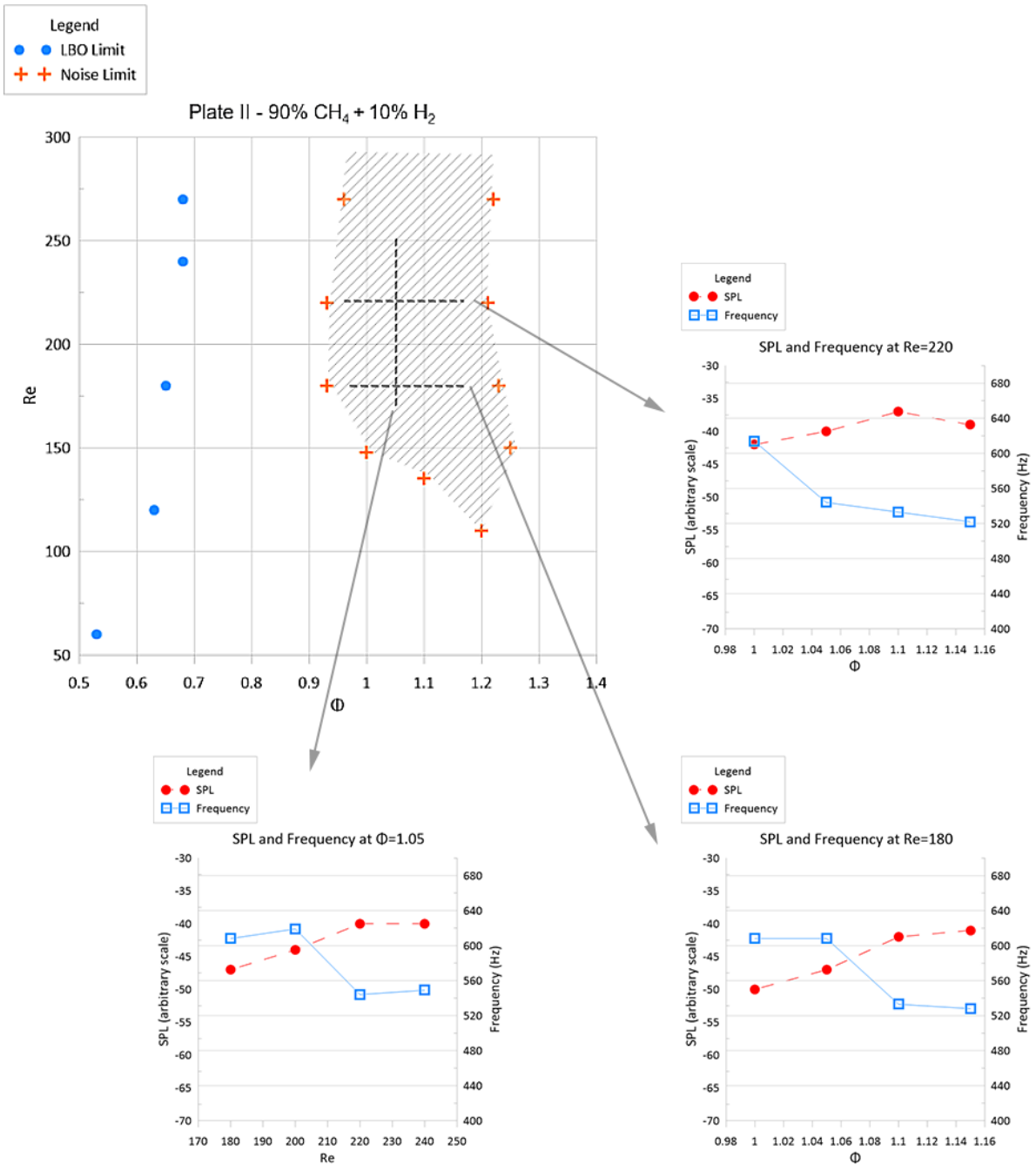

Figure 4.6: Plate II 90% CH_4 + 10% H_2 stability map at $L = 12$ cm with frequency and sound pressure level analysis for selected ϕ and Re.

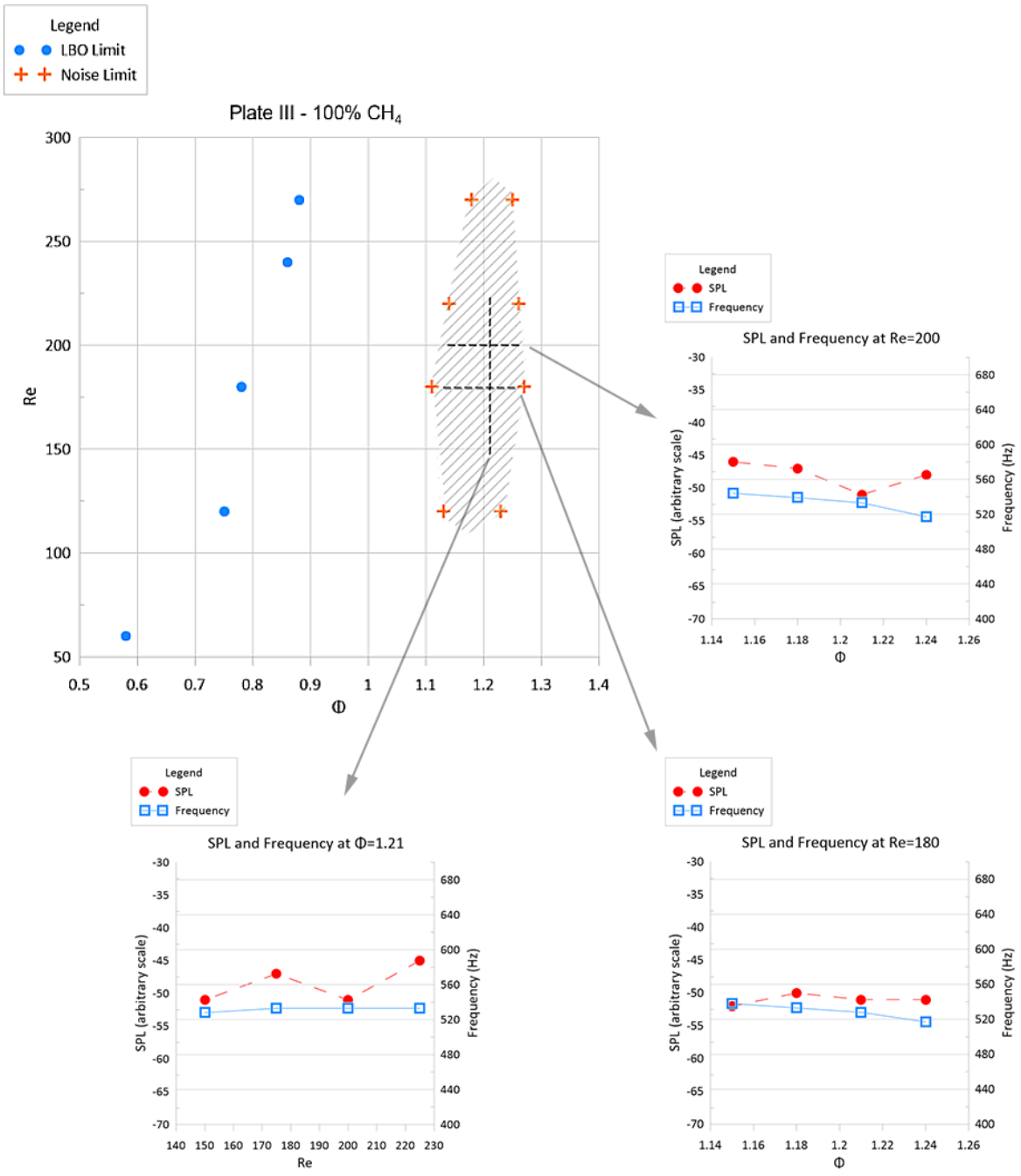

Figure 4.7: Plate III 100% CH_4 stability map at $L = 12\,\text{cm}$ with frequency and sound pressure level analysis for selected ϕ and Re.

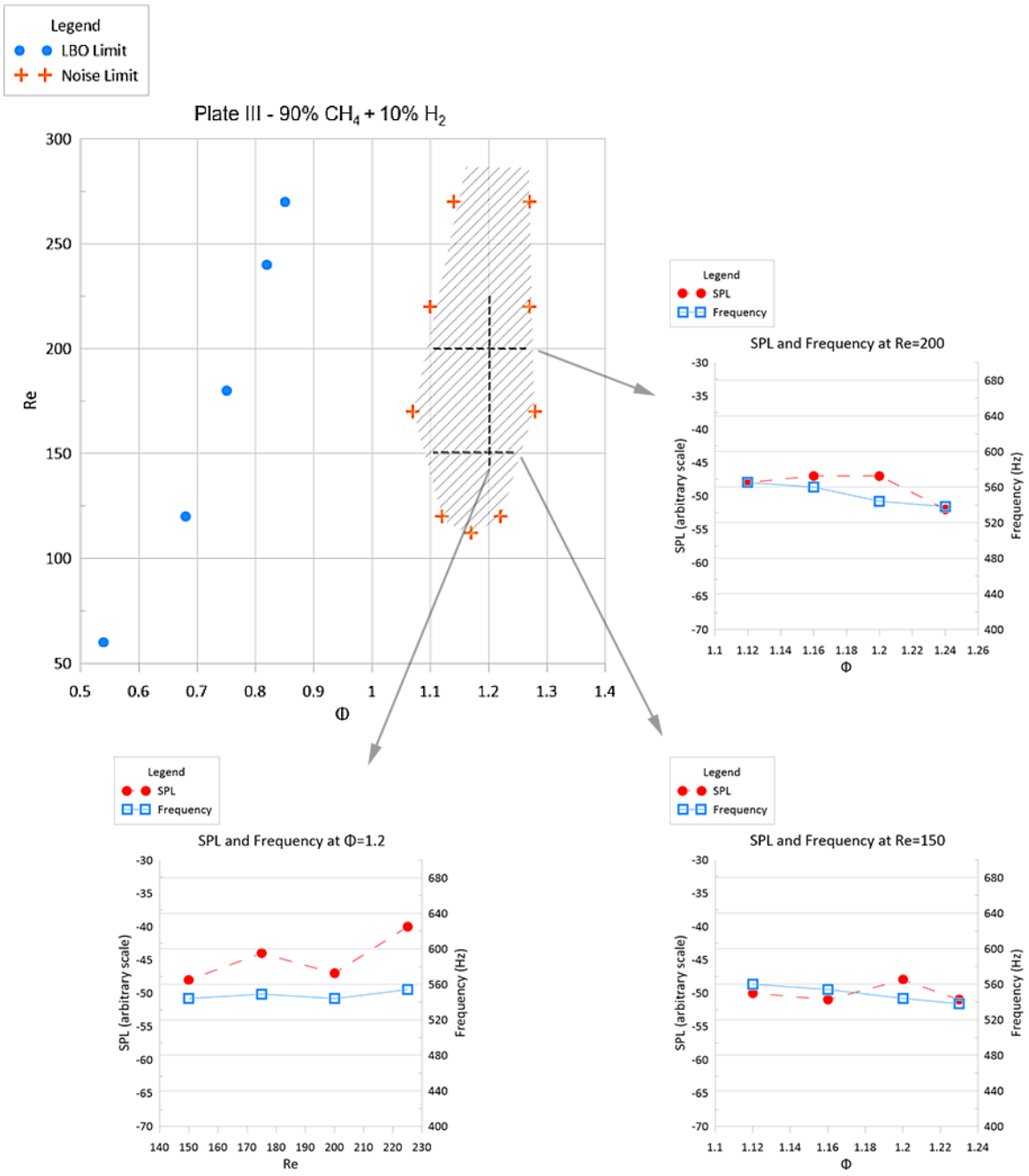

Figure 4.8: Plate III 90% CH_4 + 10% H_2 stability map at $L = 12$ cm with frequency and sound pressure level analysis for selected ϕ and Re.

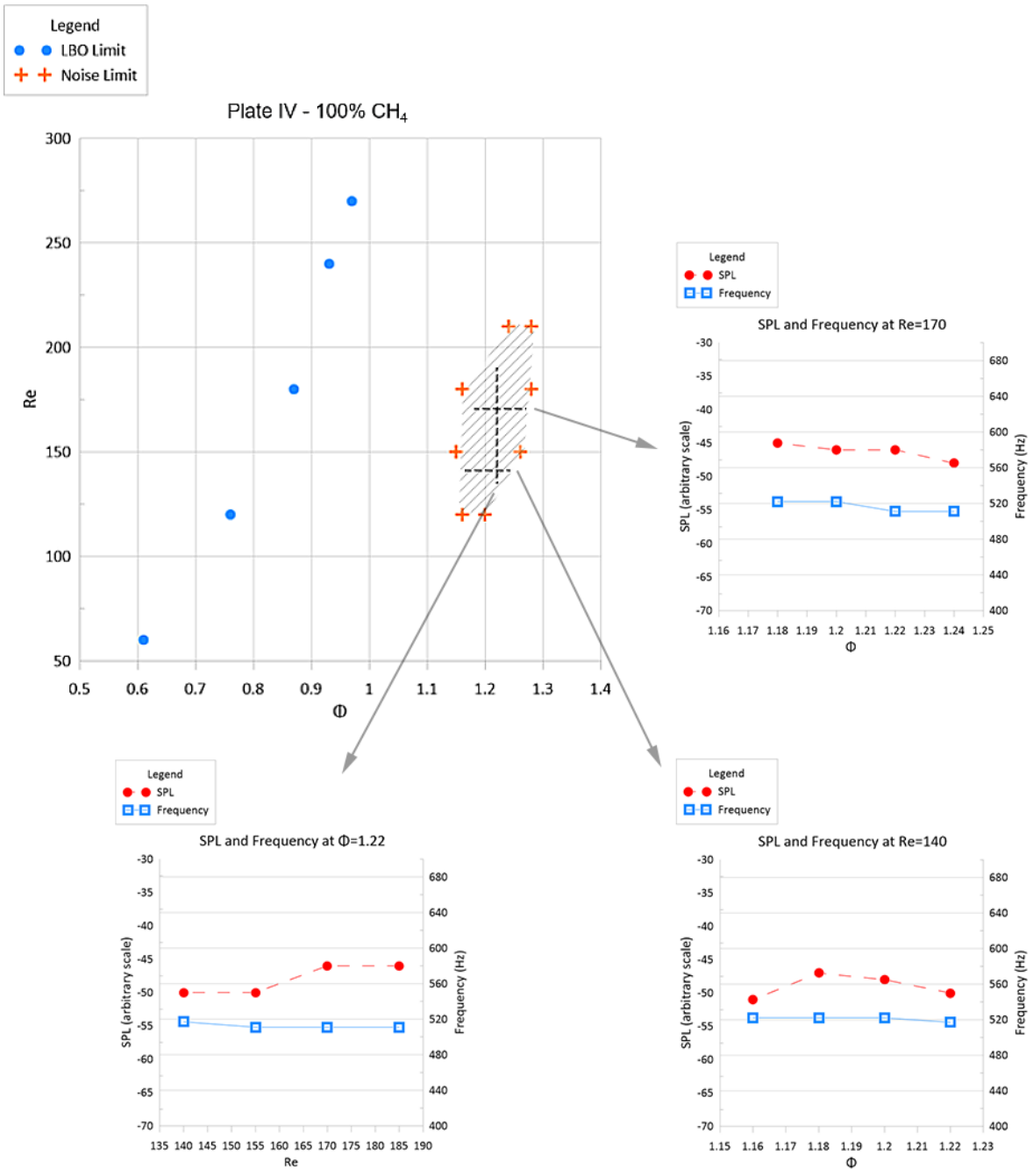

Figure 4.9: Plate IV 100% CH_4 stability map at $L = 12\,\text{cm}$ with frequency and sound pressure level analysis for selected ϕ and Re.

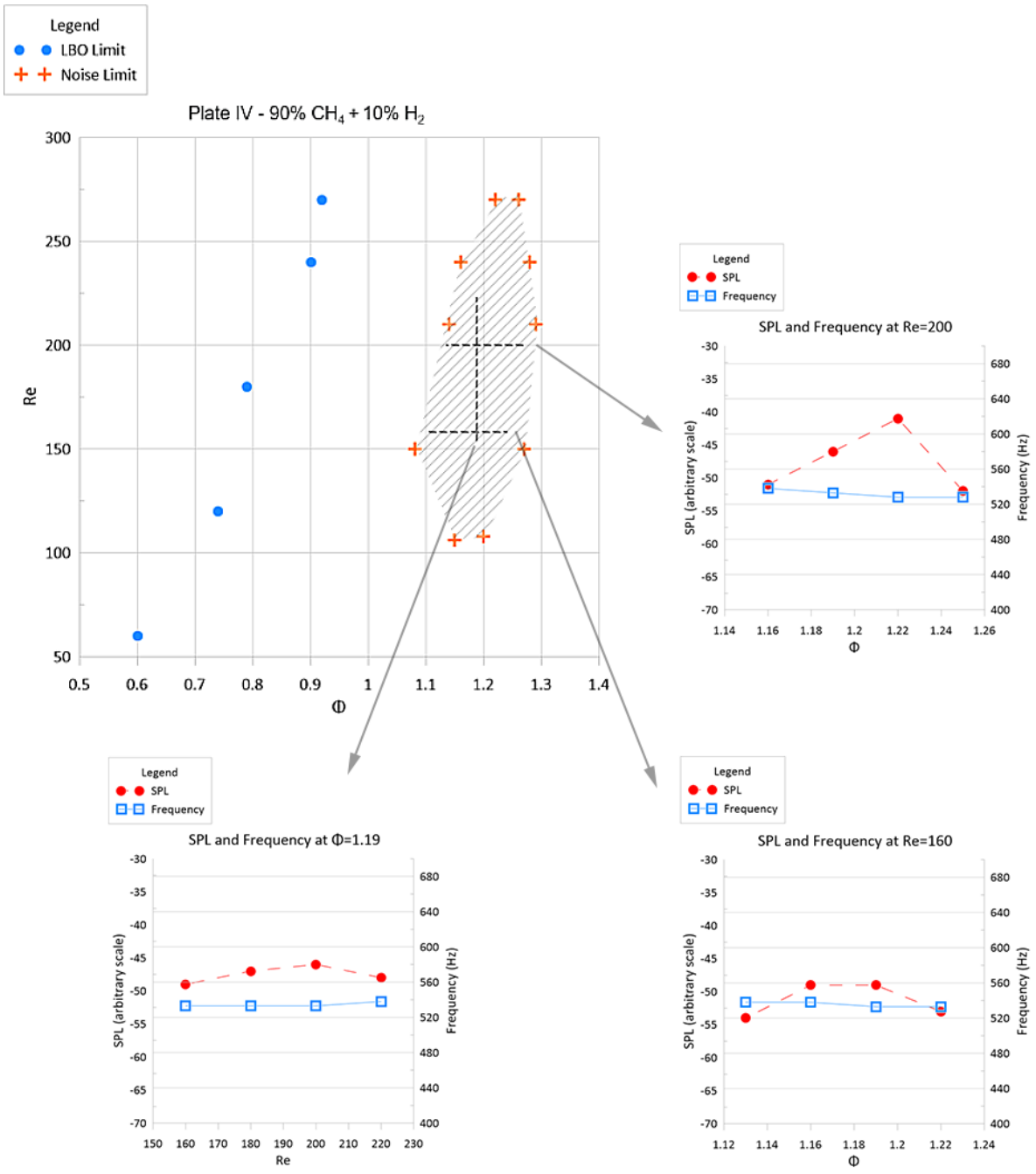

Figure 4.10: Plate IV 90% CH_4 + 10% H_2 stability map at $L = 12$ cm with frequency and sound pressure level analysis for selected ϕ and Re.

4.3 Thermoacoustic Instabilities' Flame Shape

A study of the flame shape is done in order to understand what happens to the flames when thermoacoustic instabilities exist. The different plates, from the nature of their geometry, influence the interaction between each individual flame and the addition of H_2 leads to higher flame speeds which affect the flame's shape. For that, images of the flames at unstable conditions were captured at 5000 frames per second (fps) (see figure 4.11 and 4.12) and 9009 fps (see figure 4.13). The results for the images captured at 9009 fps skip one frame for every two frames meaning that they show images as if the capture rate was of 4504.5 fps.

A common observation for all results is that the main oscillation mode is in the longitudinal direction as assumed in section 3.1. However, for $Re = 180$, $\phi = 1$ and 100% CH_4 with plate I (figure 4.11(a)) there are other relevant modes of oscillation. In this case it is possible to observe a transversal mode of oscillation, with the flames separating from each other, meaning that the first assumption made of only longitudinal modes may not always be correct. With the addition of H_2 those transversal modes are not observable, indicating that the presence H_2 can stabilize such interactions. An explanation for the particular case of $Re = 180$, $\phi = 1$ and 100% CH_4 showing transversal modes of oscillation is the interaction between each flame. Since plate I is the plate with the closest holes, the flames here have the highest possibility to interact with each other and therefore, influence each other which happens in a transversal direction. With the addition of H_2 the mixture has a higher flame speed, and therefore reduces its surface area which in turn diminishes the interactions with adjacent flames.

In the results of plate II the most iconic observation is the bubble of flame formation at the tip of the flame, a phenomena also observed in [13, 15], even though the fuels used for those studies was C_3H_8 while the ones used in this work are composed of CH_4 and H_2. In figure 4.11(c), as the flames are going down in their oscillation cycle a quantity of mixture remains at the tip and detaches from the rest of the flame, forming said bubble. This bubble then burns as the flames are already at the lower points. The addition of hydrogen shown in figure 4.11(d) makes the bubble at the tip disappear. The high flame speed induced by the presence of H_2 leads to a smaller flame area and faster burning speed which does not allow the presence of remaining mixture to be burnt and detach from the flame base. Another observation is the height and width of the flame at the lower point. In the results for 100% CH_4 the flame base is much lower than the H_2 added mixture, suggesting that the presence of H_2 makes the flame base stabler. The width of the flame shows the same behaviour, implying a reduction and less interaction between flames with the addition of H_2.

In plate IV (see figure 4.12) there are no bubbles being formed at the tip of the flame, and there is no substantial difference between the flames of 100% CH_4 and 90% CH_4 + 10% H_2 blends. The most reasonable difference shown is the flame height being taller for the former mixture. This is in agreement with previous results, as all show a lower maximum flame height with the addition of H_2.

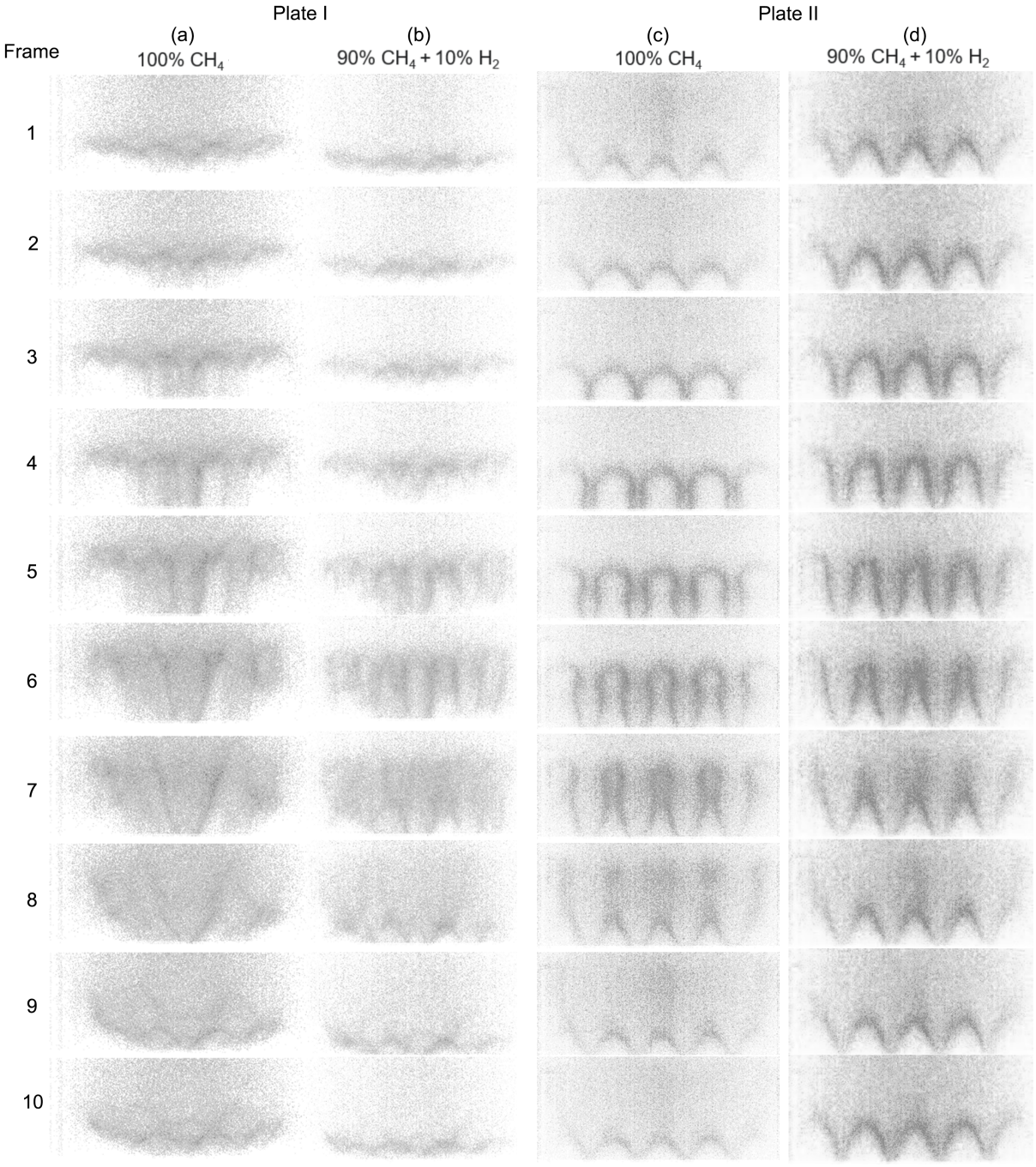

Figure 4.11: Cycle of flame oscillations at $L = 12$ cm with plates I and II captured by the high-speed camera Phantom V4.2. Time period between each frame is 0.0002s.
(a) Plate I, $Re = 180$, $\phi = 1$, $f = 528$ Hz and 100% CH_4.
(b) Plate I, $Re = 180$, $\phi = 1$, $f = 533$ Hz and 90% CH_4 + 10% H_2.
(c) Plate II, $Re = 220$, $\phi = 1$, $f = 598$ Hz and 100% CH_4.
(d) Plate II, $Re = 220$, $\phi = 1$, $f = 614$ Hz and 90% CH_4 + 10% H_2.

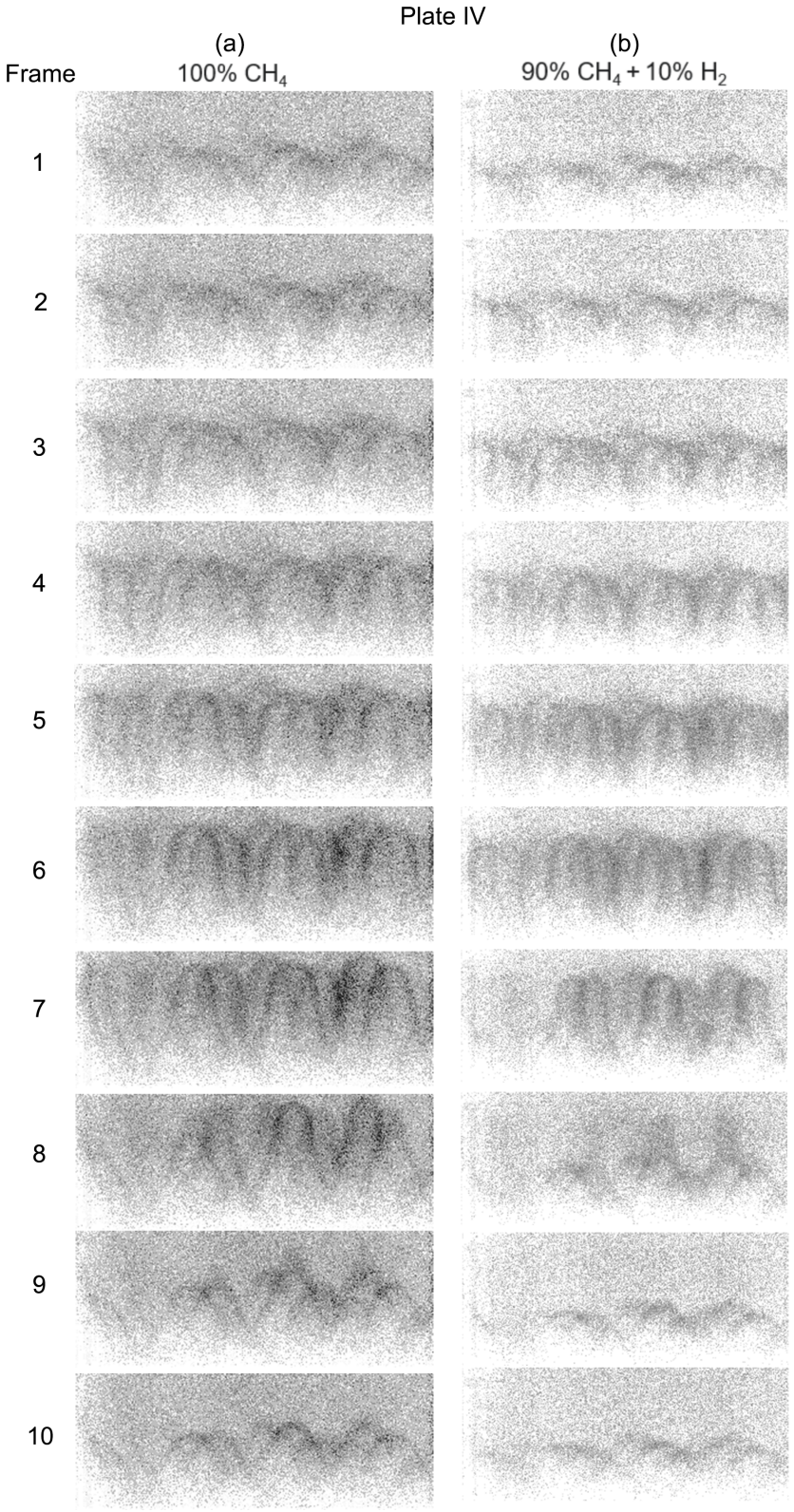

Figure 4.12: Cycle of flame oscillations at $L = 12$ cm with plate IV captured by the high-speed camera Phantom V4.2. Time period between each frame is 0.0002s.
(a) Plate IV, $Re = 170$, $\phi = 1.2$, $f = 522$ Hz and 100% CH_4.
(b) Plate IV, $Re = 170$, $\phi = 1.2$, $f = 528$ Hz and 90% CH_4 + 10% H_2.

Increase in *Re* and ϕ while keeping the same plate was done for 100% CH_4 and 90% CH_4 + 10%H_2 blends in order to evaluate the effects of *Re* and ϕ in the flame shape (see figure 4.13). It is clear that an increase in *Re* and ϕ leads to a higher flame height. If the values of such parameters are increased enough, it can even lead to the formation of bubbles as shown by the results in figure 4.13(d). Despite the mixture being composed of 90% CH_4 + 10% H_2, which implies a stabler and lower height of the flame when compared to the 100% CH_4 counterpart, the combination of a higher *Re* and ϕ leads to the detachment of mixture and flame at the tip.

Recalling the results found in section 4.2 where there is a slight increase in frequency for the H_2 enhanced blend, results show that by adding H_2 the unstable length of the flame, *i.e.* the portion of the flame that oscillates, is diminished through a combination of lower flame height and higher stable flame base, which can be an explanation for the frequency increase. This phenomena is related to the speed of sound of the mixture with the addition of H_2. As H_2 is added into the mixture, the speed of sound increases and therefore, the acoustic resonance of the burner increases (the burner acts as a Helmholtz resonator) [29]. On the other hand the lower flame height induces more gain for the FTF at higher frequencies. With the increase of oscillations at higher frequencies for both the burner and flame, thermoacoustic instabilities with higher frequencies are encouraged. Figure 4.13 also shows the same behaviour, since the flames of (a) and (b) have a shorter oscillating length due to lower *Re* and their frequencies are higher when compared to the (c) and (d) cases. The association of flame height reduction to higher resonance frequencies is also found in the literature reviewed [27, 39]. Lim *et al.* [27] reported an amplitude gains at higher frequencies with the reduction of flame height induced by the addition of H_2 in a numerical study. Altay *et al.* [39] found through an experimental analysis that as the flame's height is shortened the frequencies of resonance increase.

Another important outcome of the images is the confirmation that the noise emitted by the instabilities are associated with the oscillations visualised in a macro scale, *i.e.* the perturbations that affect the whole shape of the flame. This can be correlated since the oscillations' frequency of the flame morphology is the same as the captured sound frequencies. This is in agreement with Schuller *et al.* [18] where the fundamental frequency of the noise emitted corresponded to the flame front oscillation's frequency.

With all considered it was found that *Re*, ϕ, fuel and plate geometry influence the flame oscillations. A schematic of the various flame shapes found when thermoacoustic instabilities are present is represented in figure 4.14. The reduction of flame height and a stabilisation of the flame's base is promoted by the addition of H_2 in the blend. This leads to less interactions between flames, diminishing the transversal modes of oscillation. The increase of *Re* and ϕ leads to higher flame heights and possible flame bubble formation at the flame's tip. A larger separation between holes in the plates have the consequence of reducing the interaction between individual flames and therefore reducing their transversal influence. Another finding was the relationship between a decrease in the section of the flame that oscillates, due to a stabler flame base and lower maximum flame height, to higher frequencies.

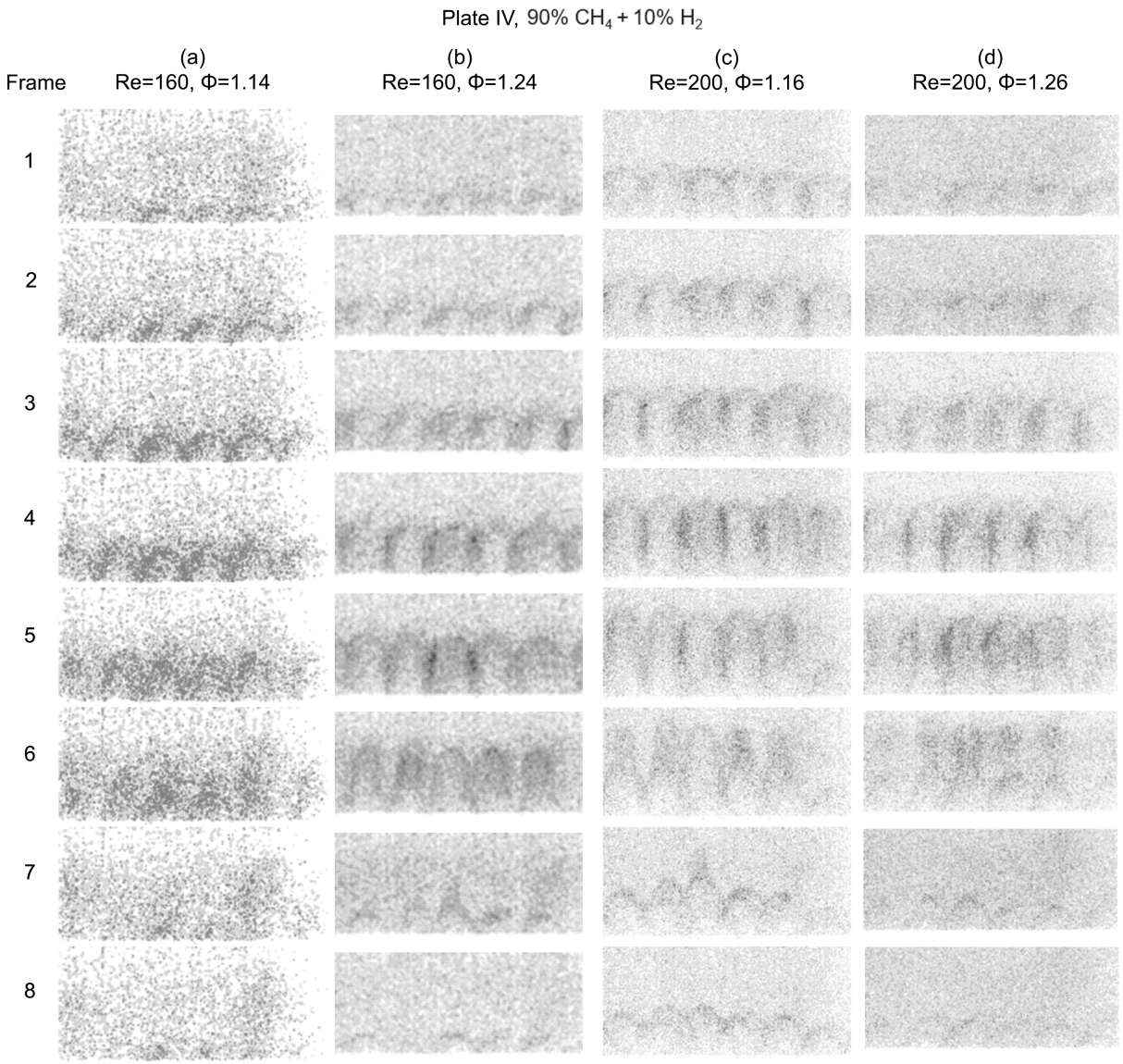

Figure 4.13: Cycle of flame oscillations at $L = 12$ cm with plate IV and 90% CH_4 + 10% H_2 captured by the high-speed camera Phantom V4.2. Time period between each frame is 0.00022s.
(a) $Re = 160$, $\phi = 1.14$, $f = 538$ Hz.
(b) $Re = 160$, $\phi = 1.24$, $f = 528$ Hz.
(c) $Re = 200$, $\phi = 1.16$, $f = 522$ Hz.
(d) $Re = 200$, $\phi = 1.26$, $f = 522$ Hz.

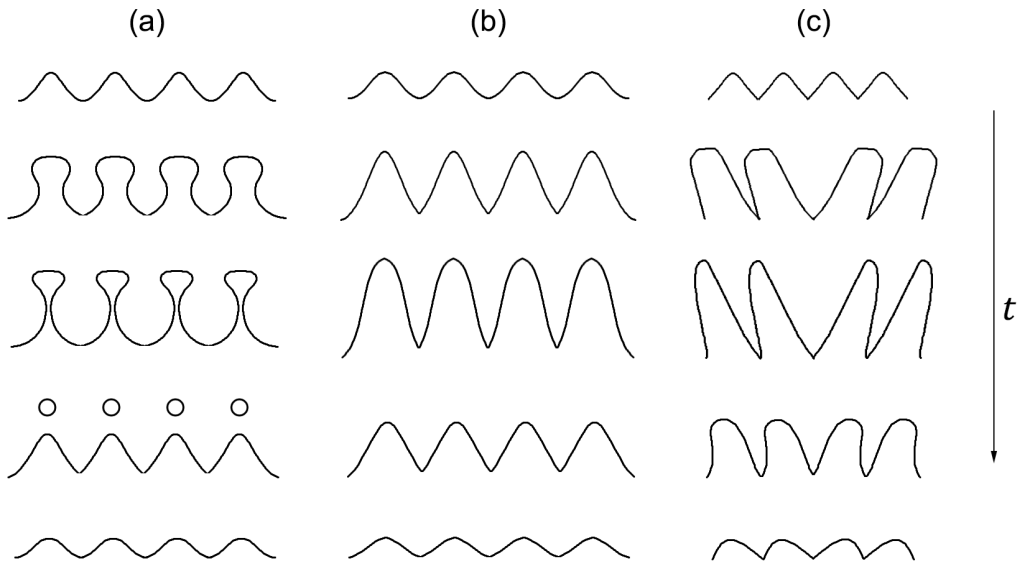

Figure 4.14: Schematics of the flame shapes found through an oscillation cycle when instabilities are present. (a) Bubble formation at the flame tip. (b) Only longitudinal mode of oscillation. (c) Presence of transversal mode of oscillation. Time goes from top to bottom.

4.4 Cavity Length Variation and Model

Until now, the evaluation of the thermoacoustic instabilities were done at a fixed cavity length of 12 cm, with no understanding of the cavity length's influence on the oscillations. To study the effects of L experiments were done with the five different plates, 100% CH_4 and 90% CH_4 + 10% H_2 fuels at fixed *Re* and ϕ conditions. Additionally, results from the mathematical model presented in chapter 3 are evaluated and compared to the experimental data.

As the cavity length L is increased, frequencies show a jumping behaviour when approaching lengths of 20 cm and above depending on the plate studied (see figures 4.15 to 4.19). Plus, the instabilities' frequencies are close to the resonance frequencies of the burner. Both of these phenomena are also found and studied in [12, 13, 15], as all show the saw-tooth behaviour of frequency with respect to L.

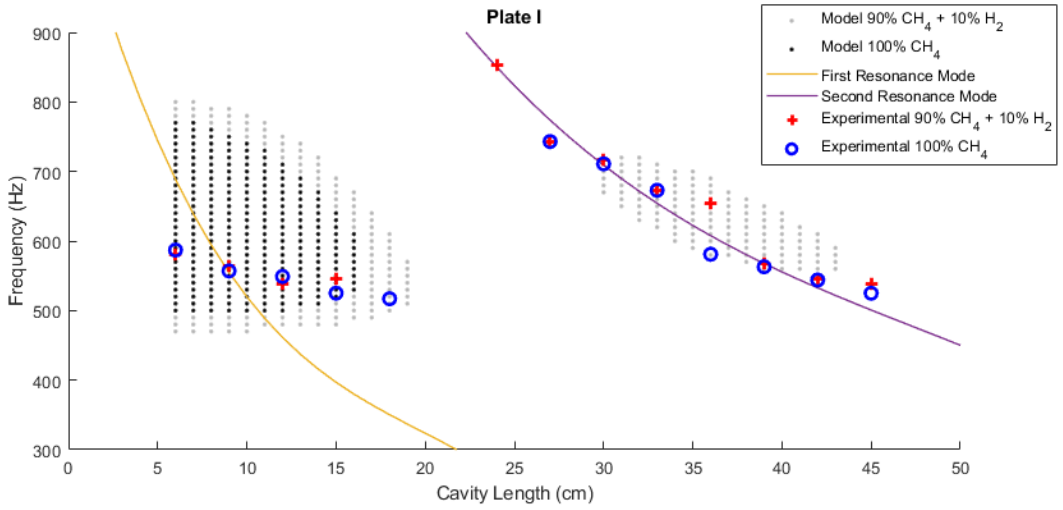

Figure 4.15: Frequencies with respect to cavity length and model results for plate I. *Re* $= 220$ and $\phi = 1$.

Observation through the plates indicates that thermoacoustic instabilities are minimized for the interval of L studied as the perforation ratio ψ decreases, specifically the reduction occurs more predominantly at higher L. This also occurs for the results obtained in [15], where the working fuel was 100% C_3H_8 and the plates were the same. In that study, the L span was from 10 to 70 cm and it was found that the instabilities are reduced with the decrease in ψ. Additionally, the reduction of instabilities also started at higher L. Considering this, removal of the instabilities at specific lengths (in this case, from around 25 cm to 35 cm) can be done by changing the plate.

No instabilities were found at fixed $L = 12\,\text{cm}$ for 100% CH_4 and 90% CH_4 + 10% H_2 with plate V previously. However, at $15\,\text{cm} \leq L \leq 21\,\text{cm}$ using the 10% H_2 fuel there are instabilities resonating at around $f = 400\,\text{Hz}$ (see figure 4.19). In these cavity lengths, the dissipative power is not enough to overcome the driving power (recall equation 3.28) and therefore noise was sustained.

Fuel wise, the H_2 enhanced mixture does seem be more prone to thermoacoustic instabilities, as the results show the presence of noise for cavity lengths in which the pure CH_4 mixture does not. This is predominant for the frequencies close to the second resonant mode, as the ones related to the first mode appear in the same quantity for both fuels in all plates besides plate V. Also, the frequencies shown for

the 90% CH_4 + 10% H_2 are slightly higher when compared to the 100% CH_4 blend, showing agreement with previous discussed results.

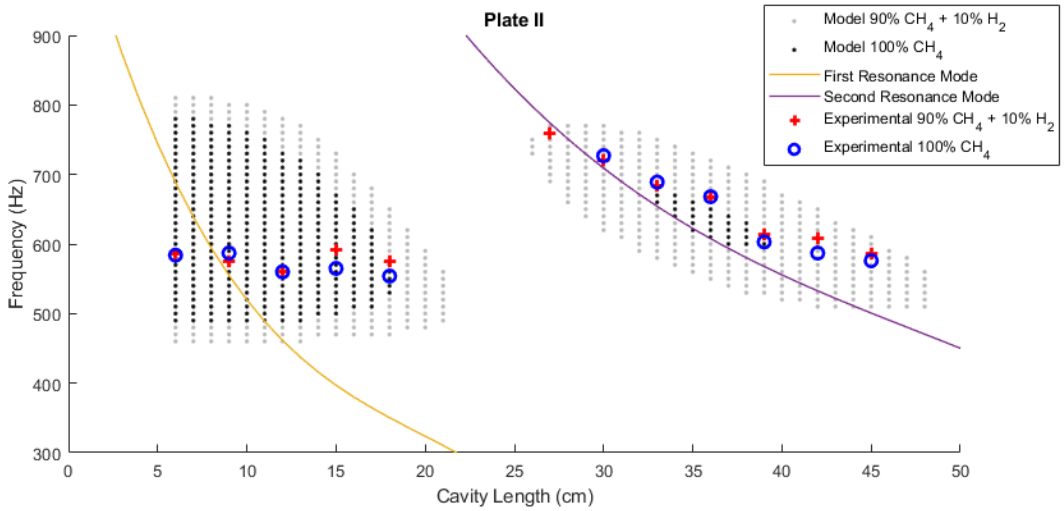

Figure 4.16: Frequencies with respect to cavity length and model results for plate II. $Re = 180$ and $\phi = 1.05$.

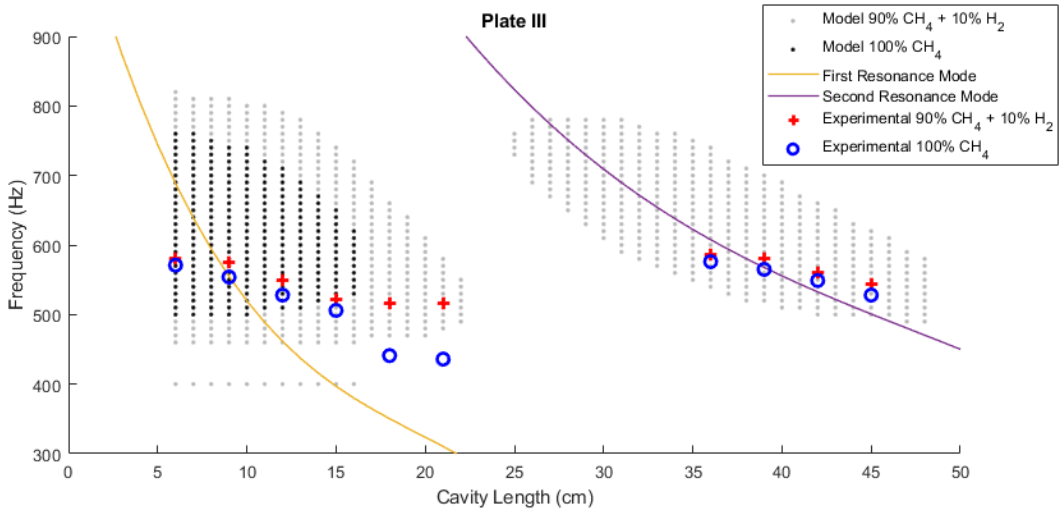

Figure 4.17: Frequencies with respect to cavity length and model results for plate III. $Re = 180$ and $\phi = 1.19$.

The noise frequencies follow the burner's resonance values only for the ones close to the second mode of resonance. The ones related to the first mode have a more monotonous behaviour with respect to L not following the steeper slope of the burner's resonance mode. This can be explained by the fact that for the burner's acoustic mode in section 3.1, it was assumed that only the longitudinal acoustic modes were relevant. However, results in section 4.3 have shown that transversal modes need also to be taken into account. Therefore, the assumption of only assuming longitudinal modes cannot be applied for shorter cavity lengths, such as the ones related to the first resonance mode.

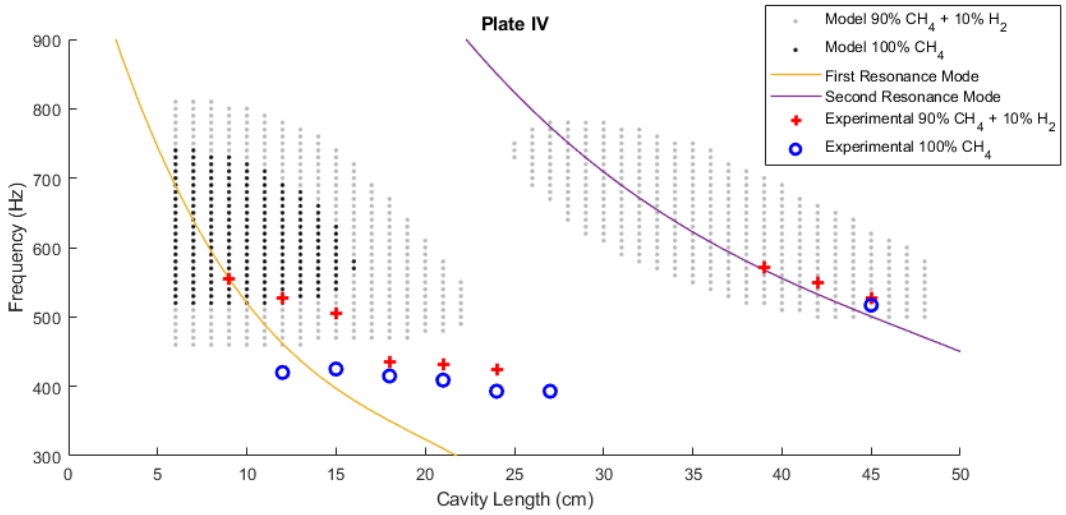

Figure 4.18: Frequencies with respect to cavity length and model results for plate IV. $Re = 170$ and $\phi = 1.2$.

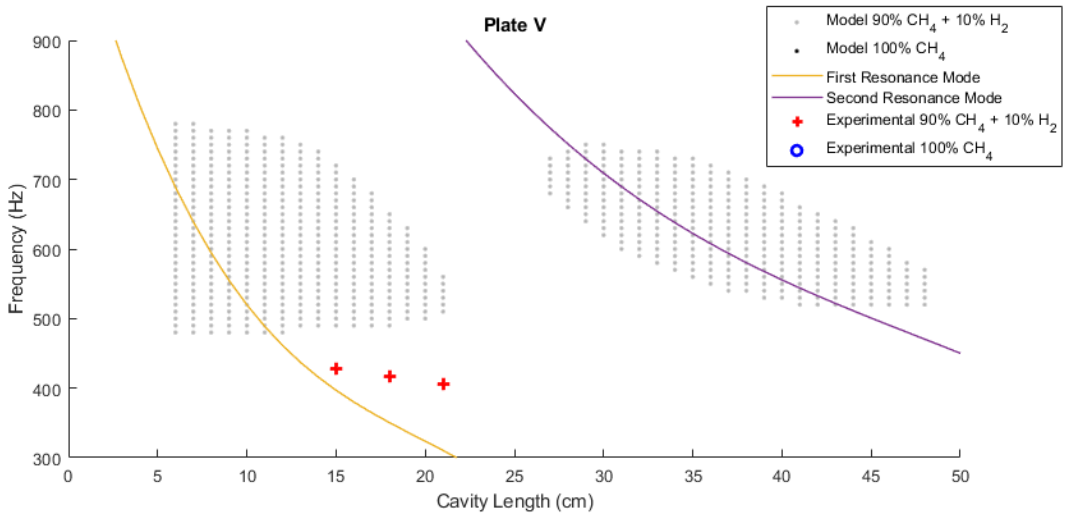

Figure 4.19: Frequencies with respect to cavity length and model results for plate V. $Re = 160$ and $\phi = 1.2$.

Lastly, the model's results show that it does not predict correctly at which length and frequencies instabilities may occur. Although for plates I and II the region where the model predicts instabilities are concurrent with the experimental data for the frequencies related to the first mode of resonance, the instabilities related to the second mode are not well predicted. This problem is further enhanced for the remaining plates, where in plate IV and V the majority of the results are shown outside the model's areas. Another observation is that the regions predicted for methane were much smaller than the hydrogen ones and reducing even more as ψ is decreased. The 90% CH_4 + 10% H_2 results did not show such expressive variations, but did show a consecutive reduction of unstable region from plate II to IV, while from plate I to II the regions increased, specially the second resonant mode one. Nevertheless, the model does indicate the jumping phenomenon of the frequencies with respect to cavity length L.

Chapter 5

Conclusions

5.1 Summary and Achievements

The objective of this thesis was to study the onset of thermoacoustic instabilities for different geometrical configurations of the burner and different fuel blends in order to evaluate the suitability of current burners for the use of H_2. With that in mind, experiments in a burner with the capability to change its cavity length were done in addition to usage of different fuel blends. The fuels evaluated were composed of 100% C_3H_8, 100% CH_4 and a mixture of 90% CH_4 + 10% H_2 (v/v). Different stabilizing plates with distinct ψ were also analysed. Information from the experiments was gathered through a microphone system and high-speed camera to evaluate the sound emitted and the flame shape respectively.

With the results from those experiments, evaluation on the influence of ϕ, *Re*, fuel composition, ψ and L on thermoacoustic instabilities were realised. Additionally, a mathematical model was demonstrated and its performance was compared to the experimental data to evaluate its viability. The relevant findings are listed below:

1. Hydrogen addition in the mixture allowed leaner operation modes. However, as the plates' holes were distanced farther apart, flames could only be sustained for richer mixtures.

2. Thermoacoustic instabilities are more prone to appear for propane mixtures when compared to the methane and hydrogen ones. Hydrogen seems to increase the probability of thermoacoustic instabilities when added to methane. A balance between LBO limits and flame stability needs to be made when choosing which plate to use.

3. It was found that the higher flame speed induced by hydrogen leads to a stabler flame base and lower flame height, this in turn conveys a shorter length for which the flame oscillates leading to a frequency increase, analogous to the reduction of clamped beam's length.

4. The modes of oscillation that dominate thermoacoustic instabilities for this burner are not only in the longitudinal direction, but also in a transversal one. High-speed camera results show that sideways oscillations of the flame are sometimes non-negligible, opposed to what was initially proposed.

5. Sometimes unburned mixture detaches from the flame tip when it is going down in the oscillation cycle, then flame bubbles are formed which burn detached from the rest of the flame. It was found that the bubbles appearance is promoted by higher *Re* and ϕ.

6. Frequencies of the oscillations were closer to the resonance of the burner alone for higher cavity lengths. This was explained due to the fact that at higher cavity lengths the approximation of only longitudinal acoustic modes was valid, but at lower lengths such assumption cannot be made as transversal modes are also relevant.

7. Although the mathematical model predicted more instabilities for the hydrogen added mixture and less instabilities as ψ decreased, its results were often far off from the experimental counterpart, showing a weak performance. Some of the possible reasons for this are the simplification of the flow inside the burner to not consider vortices formation.

5.2 Future Work

The work done in this thesis led to further understandings of thermoacoustic instabilities, specifically the effects of hydrogen, plate's separation ratio and flame shape. A mathematical model was also developed, but it had a poor performance which can be further improved. The findings of this thesis can be used as a guideline for future developments on the subject such as:

1. Addition of higher hydrogen fractions to the mixture to understand if the fuel has a linear behaviour of always increasing thermoacoustic instabilities, or if there is a point from which the instabilities are diminished.

2. Analysis of new plate configurations with different hole shapes and sizes in order to find their effects on the onset of the instabilities. Plate geometry wise, the study focused only on the perforation ratio. However, different flame shapes induced by different hole shapes may trigger other behaviours in the thermoacoustic instabilities. Another possibility is the study of two MPPs in series to increase the damping factor of the burner to try minimizing the thermoacoustic instabilities.

3. Evaluation of the mathematical model in a detailed form in order to improve its performance. The model proposed in this work had assumptions that were found to be incorrect and was based on previous work done by Ferreira [15], where the FTF used was based on propane flames calculated by Leitão [38]. Obtaining new FTF for mixtures with hydrogen fractions and considering transversal modes of oscillation is necessary to further develop the model. Furthermore, considering that the model was simplified, it may be required to use a numerical model instead of the analytical one presented here.

Bibliography

[1] M. Hoeijmakers, V. Kornilov, I. Lopez Arteaga, P. de Goey, and H. Nijmeijer. Intrinsic instability of flame–acoustic coupling. *Combustion and Flame*, 161(11):2860–2867, 2014. doi: 10.1016/j.combustflame.2014.05.009.

[2] A. Birbaud, D. Durox, S. Ducruix, and S. Candel. Dynamics of confined premixed flames submitted to upstream acoustic modulations. *Proceedings of the Combustion Institute*, 31(1):1257–1265, 2007. ISSN 1540-7489. doi: https://doi.org/10.1016/j.proci.2006.07.122.

[3] T. Schuller, D. Durox, and S. Candel. Dynamics of and noise radiated by a perturbed impinging premixed jet flame. *Combustion and Flame*, 128(1):88–110, 2002. ISSN 0010-2180. doi: https://doi.org/10.1016/S0010-2180(01)00334-0.

[4] D. Durox, T. Schuller, and S. Candel. Self-induced instability of a premixed jet flame impinging on a plate. *Proceedings of the Combustion Institute*, 29(1):69–75, 2002. ISSN 1540-7489. doi: https://doi.org/10.1016/S1540-7489(02)80013-X. Proceedings of the Combustion Institute.

[5] NASA. Apollo era testing. `https://www1.grc.nasa.gov/historic-facilities/rocket-engine-test-facility/apollo-era-testing/#lightbox-gallery-1-6`, 2018. Accessed: 2021-09-13.

[6] J. C. Oefelein and V. Yang. Comprehensive review of liquid-propellant combustion instabilities in f-1 engines. *Journal of Propulsion and Power*, 9(5):657–677, 1993. doi: 10.2514/3.23674.

[7] L. Rayleigh. The explanation of certain acoustical phenomena. *Nature*, 18(455):319–321, 1878. doi: 10.1038/018319a0.

[8] P. L. Rijke. Notiz über eine neue art, die in einer an beiden enden offenen röhre enthaltene luft in schwingungen zu versetzen. *Annalen der Physik*, 183(6):339–343, 1859. doi: https://doi.org/10.1002/andp.18591830616.

[9] J. Moeck, M. Oevermann, R. Klein, C. Paschereit, and H. Schmidt. A two-way coupling for modeling thermoacoustic instabilities in a flat flame rijke tube. *Proceedings of the Combustion Institute*, 32 (1):1199–1207, 2009. ISSN 1540-7489. doi: https://doi.org/10.1016/j.proci.2008.05.062.

[10] A. A. Putnam and W. R. Dennis. Organ-pipe oscillations in a flame-filled tube. *Symposium (International) on Combustion*, 4(1):566–575, 1953. ISSN 0082-0784. doi: https://doi.org/10.1016/S0082-0784(53)80078-0. Fourth Symposium (International) on Combustion.

[11] B. T. Zinn. Pulse combustion: recent applications and research issues. *Symposium (International) on Combustion*, 24(1):1297–1305, 1992. ISSN 0082-0784. doi: https://doi.org/10.1016/S0082-0784(06)80151-7. Twenty-Fourth Symposium on Combustion.

[12] N. Noiray, D. Durox, T. Schuller, and S. Candel. Self-induced instabilities of premixed flames in a multiple injection configuration. *Combustion and Flame*, 145(3):435–446, 2006. ISSN 0010-2180. doi: https://doi.org/10.1016/j.combustflame.2006.01.006.

[13] N. Noiray, D. Durox, T. Schuller, and S. Candel. Passive control of combustion instabilities involving premixed flames anchored on perforated plates. *Proceedings of the Combustion Institute*, 31(1):1283–1290, 2007. ISSN 1540-7489. doi: https://doi.org/10.1016/j.proci.2006.07.096.

[14] J. Correia. Modelação matemática e experimental das instabilidades termoacústicas de estabilizadores de chama do tipo chapa multi-perforada. Master's thesis, Instituto Superior Técnico, November 2011.

[15] M. Ferreira. Thermoacoustic self-sustained instabilities of conical flames in multi-perforated plate burners. Master's thesis, Instituto Superior Técnico, July 2017.

[16] D.-Y. Maa. Potential of microperforated panel absorber. *The Journal of the Acoustical Society of America*, 104(5):2861–2866, 1998. doi: 10.1121/1.423870.

[17] E. Fernandes and R. Leandro. Modeling and experimental validation of unsteady impinging flames. *Combustion and Flame*, 146(4):674–686, 2006. ISSN 0010-2180. doi: https://doi.org/10.1016/j.combustflame.2006.06.008.

[18] T. Schuller, D. Durox, and S. Candel. Self-induced combustion oscillations of laminar premixed flames stabilized on annular burners. *Combustion and Flame*, 135(4):525–537, 2003. ISSN 0010-2180. doi: https://doi.org/10.1016/j.combustflame.2003.08.007.

[19] T. Schuller, D. Durox, and S. Candel. A unified model for the prediction of laminar flame transfer functions: comparisons between conical and v-flame dynamics. *Combustion and Flame*, 134(1):21–34, 2003. ISSN 0010-2180. doi: https://doi.org/10.1016/S0010-2180(03)00042-7.

[20] United Nations. The Paris Agreement. `https://unfccc.int/process-and-meetings/the-paris-agreement/the-paris-agreement`. Accessed: 2021-12-04.

[21] P. Chiesa, G. Lozza, and L. Mazzocchi. Using Hydrogen as Gas Turbine Fuel . *Journal of Engineering for Gas Turbines and Power*, 127(1):73–80, 02 2005. ISSN 0742-4795. doi: 10.1115/1.1787513.

[22] A. Lantz, R. Collin, M. Aldén, A. Lindholm, J. Larfeldt, and D. Lörstad. Investigation of Hydrogen Enriched Natural Gas Flames in a SGT-700/800 Burner Using OH PLIF and Chemiluminescence

Imaging. *Journal of Engineering for Gas Turbines and Power*, 137(3):031505, Mar. 2015. ISSN 0742-4795, 1528-8919. doi: 10.1115/1.4028462.

[23] P. Griebel, E. Boschek, and P. Jansohn. Lean Blowout Limits and NO Emissions of Turbulent, Lean Premixed, Hydrogen-Enriched Methane/Air Flames at High Pressure. *Journal of Engineering for Gas Turbines and Power-transactions of The Asme - J ENG GAS TURB POWER-T ASME*, 129, 04 2007. doi: 10.1115/1.2436568.

[24] J. Runyon. *Gas Turbine Fuel Flexibility: Pressurized Swirl Flame Stability, Thermoacoustics, and Emissions*. PhD thesis, University of Cardiff, May 2017.

[25] A. Palacios and D. Bradley. Conversion of natural gas jet flame burners to hydrogen. *International Journal of Hydrogen Energy*, 46(33):17051–17059, May 2021. ISSN 03603199. doi: 10.1016/j.ijhydene.2021.02.144.

[26] D. R. Jones and C. W. Dunnill. On the initiation of blow-out from cooktop burner jets: A simplified energy-based description for the onset of laminar flame extinction in premixed hydrogen-enriched natural gas (heng) systems. *Fuel*, 294:120527, June 2021. ISSN 00162361. doi: 10.1016/j.fuel.2021.120527.

[27] Z. Lim, J. Li, and A. S. Morgans. The effect of hydrogen enrichment on the forced response of CH4/H2/Air laminar flames. *International Journal of Hydrogen Energy*, 46(46):23943–23953, 2021. ISSN 0360-3199. doi: https://doi.org/10.1016/j.ijhydene.2021.04.171.

[28] E. Karlis, Y. Liu, Y. Hardalupas, and A. M. Taylor. H2 enrichment of CH4 blends in lean premixed gas turbine combustion: An experimental study on effects on flame shape and thermoacoustic oscillation dynamics. *Fuel*, 254:115524, Oct. 2019. ISSN 00162361. doi: 10.1016/j.fuel.2019.05.107.

[29] D. Kim, S. Joo, and Y. Yoon. Effects of fuel line acoustics on the self-excited combustion instability mode transition with hydrogen-enriched laboratory-scale partially premixed combustor. *International Journal of Hydrogen Energy*, 45(38):19956–19964, 2020. ISSN 0360-3199. doi: https://doi.org/10.1016/j.ijhydene.2020.05.074.

[30] D. G. Goodwin, R. L. Speth, H. K. Moffat, and B. W. Weber. Cantera: An object-oriented software toolkit for chemical kinetics, thermodynamics, and transport processes. `https://www.cantera.org`, 2021. Version 2.5.1.

[31] Gregory P. Smith, David M. Golden, Michael Frenklach, Nigel W. Moriarty, Boris Eiteneer, Mikhail Goldenberg, C. Thomas Bowman, Ronald K. Hanson, Soonho Song, William C. Gardiner, Jr., Vitali V. Lissianski, and Zhiwei Qin. GRI-MECH 3.0. `http://www.me.berkeley.edu/gri_mech/`.

[32] E. C. Fernandes. *The Onset of Combustion-Driven Acoustic Oscillation*. PhD thesis, Instituto Superior Técnico, 1998.

[33] H. Tijdeman. On the propagation of sound waves in cylindrical tubes. *Journal of Sound and Vibration*, 39(1):1–33, 1975. ISSN 0022-460X. doi: https://doi.org/10.1016/S0022-460X(75)80206-9.

[34] M. A. Temiz, J. Tournadre, I. L. Arteaga, and A. Hirschberg. Non-linear acoustic transfer impedance of micro-perforated plates with circular orifices. *Journal of Sound and Vibration*, 366:418–428, 2016. ISSN 0022-460X. doi: https://doi.org/10.1016/j.jsv.2015.12.022.

[35] A. Poludnenko and E. Oran. The interaction of high-speed turbulence with flames: Turbulent flame speed. *Combustion and Flame*, 158(2):301–326, 2011. ISSN 0010-2180. doi: https://doi.org/10.1016/j.combustflame.2010.09.002.

[36] F. M. Quintino and E. C. Fernandes. Numerical Investigation of the Impact of H2 Enrichment on Lean Biogas/Air Flames: An Analytical Modelling Approach. *Energies*, 14(2):369, Jan. 2021. ISSN 1996-1073. doi: 10.3390/en14020369.

[37] F. Coppens, J. De Ruyck, and A. Konnov. Effects of hydrogen enrichment on adiabatic burning velocity and no formation in methane+air flames. *Experimental Thermal and Fluid Science*, 31(5): 437–444, 2007. ISSN 0894-1777. doi: https://doi.org/10.1016/j.expthermflusci.2006.04.012. Fourth Mediterranean Combustion Symposium.

[38] I. D. V. Leitão. Experimental and analytical flame transfer functions of multi-perforated plate burners. Master's thesis, Instituto Superior Técnico, September 2009.

[39] H. Altay, S. Park, D. Wu, D. Wee, A. Annaswamy, and A. Ghoniem. Modeling the dynamic response of a laminar perforated-plate stabilized flame. *Proceedings of the Combustion Institute*, 32(1):1359–1366, 2009. ISSN 1540-7489. doi: https://doi.org/10.1016/j.proci.2008.06.099.

Appendix A

Difference in Side of Plates' Perforations

The plates' holes were fabricated with laser cutting techniques, since it has a smoother surface when compared with drilling techniques. Experiments reveal that both sides of the plates have slightly different results for the onset of thermoacoustic instabilities. Verification of the holes' diameters were done with confocal laser scanning microscopy by Ferreira [15] and a small difference between both sides of the same hole were found. For plate I, the side with a halo around the holes had a reduction of 6% in diameter when compared with the opposite side (see figure A.1). The effective hole diameter of the plates is taken into account in the energy balance calculations.

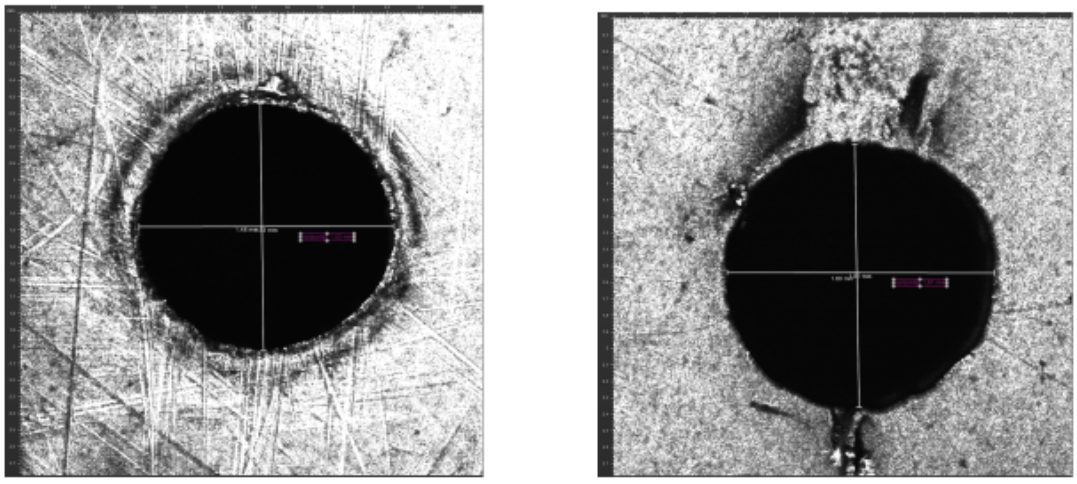

Figure A.1: Plate I hole's image captured with confocal laser scanning microscopy. Left side: halo around the hole (less 6% diameter). Right side: opposite side of the same perforation. [15]

Appendix B

Tijdeman Solution for sound propagation in cylindrical tubes

Deduction of the Low Reduced Frequency method done by Tijdeman [33].

The equations that describe the movement of a fluid inside a cylinder ar the Navier Stokes equations (axial and radial directions), the continuity equation, ideal gas law and energy equation that represents the balance of kinetic and thermal energy.

The Navier Stokes equations:

$$\rho\left[\frac{\partial u}{\partial t}+v\frac{\partial u}{\partial r}+u\frac{\partial u}{\partial x}\right]=-\frac{\partial p}{\partial x}+\mu\left[\left(\frac{\partial^2 u}{\partial x^2}+\frac{\partial^2 u}{\partial r^2}+\frac{1}{r}\frac{\partial u}{\partial r}\right)+\frac{1}{3}\frac{\partial}{\partial x}\left(\frac{\partial u}{\partial x}+\frac{\partial v}{\partial r}+\frac{v}{r}\right)\right] \tag{B.1}$$

$$\rho\left[\frac{\partial u}{\partial t}+v\frac{\partial u}{\partial r}+u\frac{\partial u}{\partial x}\right]=-\frac{\partial p}{\partial r}+\mu\left[\left(\frac{\partial^2 u}{\partial r^2}+\frac{\partial^2 u}{\partial x^2}+\frac{1}{r}\frac{\partial v}{\partial r}-\frac{v}{r^2}\right)+\frac{1}{3}\frac{\partial}{\partial r}\left(\frac{\partial u}{\partial x}+\frac{\partial v}{\partial r}+\frac{v}{r}\right)\right] \tag{B.2}$$

Continuity equation follows as:

$$\frac{\partial \rho}{\partial t}+u\frac{\partial \rho}{\partial x}+v\frac{\partial \rho}{\partial r}+\rho\left[\frac{\partial u}{\partial x}+\frac{\partial v}{\partial r}+\frac{v}{r}\right] \tag{B.3}$$

The idea gas law is:

$$p=\rho R_0 T \tag{B.4}$$

Energy equation:

$$\rho C_p\left(\frac{\partial T}{\partial t}+u\frac{\partial T}{\partial x}+v\frac{\partial T}{\partial r}\right)=\lambda\left(\frac{\partial^2 T}{\partial r^2}+\frac{\partial^2 T}{\partial x^2}p\frac{1}{r}\frac{\partial T}{\partial r}\right)+\frac{\partial \rho}{\partial t}+u\frac{\partial \rho}{\partial x}+v\frac{\partial rho}{\partial r}+\mu\phi \tag{B.5}$$

In which ϕ represents the dissipation of energy due to friction of the fluid within the walls of the tube:

$$\phi=2\left[\left(\frac{\partial u}{\partial x}\right)^2+\left(\frac{\partial v}{\partial r}\right)^2+\left(\frac{v}{r}\right)^2\right]+\left(\frac{\partial v}{\partial x}+\frac{\partial u}{\partial r}\right)^2-\frac{2}{3}\left(\frac{\partial u}{\partial x}+\frac{\partial v}{\partial r}+\frac{v}{r}\right)^2 \tag{B.6}$$

Taking into account:

$$u = c\tilde{u}(x,y)e^{i\omega t} \tag{B.7}$$

$$v = c\tilde{v}(x,r)e^{i\omega t} \tag{B.8}$$

$$p = p_s(1 + p\tilde{p}(x,r)e^{i\omega t}) \tag{B.9}$$

$$\rho = \rho_s(1 + \tilde{\rho}(x,r)e^{i\omega t}) \tag{B.10}$$

$$T = T_s(1 + \tilde{T}(x,r)e^{i\omega t}) \tag{B.11}$$

Where $\tilde{u}$, $\tilde{v}$, $\tilde{p}$, $\tilde{\rho}$ and $\tilde{T}$ are the small sinusoidal perturbations of their respective mean values. Introducing the dimensionless coordinates from figure B.1:

$$\xi = \frac{\omega x}{c} \quad \text{and} \quad \eta = \frac{r}{R} \tag{B.12}$$

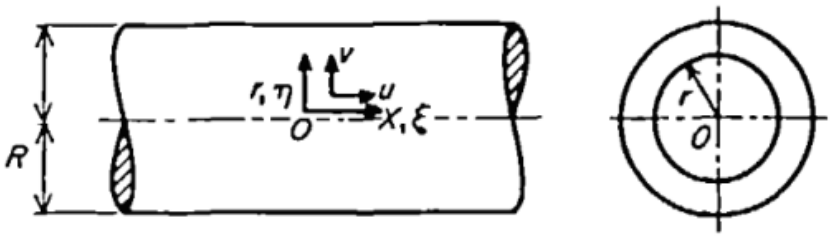

Figure B.1: Coordinate system (x,r) and the dimensionless coordinate system (ξ,η).

The equations B.1 to B.5 can be re-written as:

$$i\tilde{u} = -\frac{1}{\gamma}\frac{\partial\tilde{p}}{\partial\xi} + \frac{\mu}{\rho_s\omega R^2}\left[\left(\left(\frac{\omega R}{c}\right)^2\frac{\partial^2\tilde{u}}{\partial\xi^2} + \frac{\partial^2\tilde{u}}{\partial\eta^2} + \frac{1}{\eta}\frac{\partial\tilde{u}}{\partial\eta}\right) + \frac{1}{3}\left(\frac{\omega R}{c}\right)\frac{\partial}{\partial\xi}\left(\left(\frac{\omega R}{c}\right)\frac{\partial\tilde{u}}{\partial xi} + \frac{\partial\tilde{v}}{\partial\eta} + \frac{\tilde{v}}{\eta}\right)\right] \tag{B.13}$$

$$i\tilde{v} = -\frac{1}{\gamma}\left(\frac{c}{\omega R}\right)\frac{\partial\tilde{p}}{\partial\eta} + \frac{\mu}{\rho_s\omega R^2}\left[\left(\frac{\partial^2\tilde{v}}{\partial\eta^2} + \left(\frac{\omega R}{c}\right)^2\frac{\partial^2\tilde{v}}{\partial\xi^2} + \frac{1}{\eta}\frac{\partial\tilde{v}}{\partial\eta} - \frac{\tilde{v}}{\eta^2}\right) + \frac{1}{3}\left(\frac{\omega R}{c}\right)\frac{\partial}{\partial\xi}\left(\left(\frac{\omega R}{c}\right)\frac{\partial\tilde{u}}{\partial xi} + \frac{\partial\tilde{v}}{\partial\eta} + \frac{\tilde{v}}{\eta}\right)\right] \tag{B.14}$$

$$i\tilde{\rho} = -\left(\frac{c}{\omega R}\right)\left[\left(\frac{\omega R}{c}\right)\frac{\partial\tilde{u}}{\partial\xi} + \frac{\partial\tilde{v}}{\partial\eta} + \frac{\tilde{v}}{\eta}\right] \tag{B.15}$$

$$\tilde{p} = \tilde{\rho}\tilde{T} \tag{B.16}$$

$$i\tilde{T} = \left(\frac{\lambda}{\mu C_p}\right)\left(\frac{\mu}{\rho_s\omega R^2}\right)\left[\frac{\partial^2\tilde{T}}{\partial\eta^2} + \frac{1}{\eta}\frac{\partial\tilde{T}}{\partial\eta} + \left(\frac{\omega R}{c}\right)^2\frac{\partial^2\tilde{T}}{\partial\xi^2}\right] + i\frac{\gamma-1}{\gamma}\tilde{p} \tag{B.17}$$

From the equations above, four parameters can be identified:

Shear wave number, $$s = r\sqrt{\frac{\rho_s\omega}{\mu}} \tag{B.18}$$

Reduced frequency number, $$k = \frac{\omega r}{c} \tag{B.19}$$

Square root of the Prandtl number, $$\sigma = \sqrt{\frac{\mu C_P}{\kappa}} \tag{B.20}$$

Specific heats ratio, $$\gamma = \frac{C_P}{C_V} \tag{B.21}$$

Therefore, we can simplify the aforementioned equations to:

$$i\tilde{u} = -\frac{1}{\gamma}\frac{\partial \tilde{p}}{\partial \xi} + \frac{1}{s^2}\left[\left(k^2\frac{\partial^2 \tilde{u}}{\partial \xi^2} + \frac{\partial^2 \tilde{u}}{\partial \eta^2} + \frac{1}{\eta}\frac{\partial \tilde{u}}{\partial \eta}\right) + \frac{1}{3}k\frac{\partial}{\partial \xi}\left(k\frac{\partial \tilde{u}}{\partial \xi} + \frac{\partial \tilde{v}}{\partial \eta} + \frac{\tilde{v}}{\eta}\right)\right] \tag{B.22}$$

$$ik\tilde{v} = -\frac{1}{\gamma}\frac{\partial \tilde{p}}{\partial \eta} + \frac{k}{s^2}\left[\left(\frac{\partial^2 \tilde{v}}{\partial \eta^2} + k^2\frac{\partial^2 \tilde{v}}{\partial \xi^2} + \frac{1}{\eta}\frac{\partial \tilde{v}}{\partial \eta} - \frac{\tilde{v}}{\eta^2}\right) + \frac{1}{3}\frac{\partial}{\partial \xi}\left(k\frac{\partial \tilde{u}}{\partial \xi} + \frac{\partial \tilde{v}}{\partial \eta} + \frac{\tilde{v}}{\eta}\right)\right] \tag{B.23}$$

$$ik\tilde{\rho} = -\left[k\frac{\partial \tilde{u}}{\partial \xi} + \frac{\partial \tilde{v}}{\partial \eta} + \frac{\tilde{v}}{\eta}\right] \tag{B.24}$$

$$i\tilde{T} = \frac{1}{\sigma^2 s^2}\left[\frac{\partial^2 \tilde{T}}{\partial eta^2} + \frac{1}{\eta}\frac{\partial \tilde{T}}{\partial \eta} + k^2\frac{\partial^2 \tilde{T}}{\partial \xi^2}\right] + i\frac{\gamma - 1}{\gamma}\tilde{p} \tag{B.25}$$

Assuming the following statements:

- the air is a homogenous medium, which means that the wave length and the tube radius must be large in comparison with the mean free path, for standard temperature and pressure, this conditions breaks down for $f > 10^8$ Hz and $R < 10^{-6}$ mm
- no steady flow
- small amplitude sinusoidal perturbations, without circulation nor turbulence
- long tube, so that end effect is negligible

The solution for a rigid tube of constant circular cross-section has equations B.22 to B.25 satisfy the following boundary conditions:

- at the tube wall, the axial and radial velocity is zero: at $\eta = 1$, $\tilde{u} = 0$ and $\tilde{v} = 0$
- the radial velocity component must be zero at the tube axis due to the axis-symmetry of the problem: at $\eta = 0$, $\tilde{v} = 0$
- heat conductivity of the tube wall is larger in comparison with the heat conductivity of the fluid: at $\eta = 1$, $\tilde{T} = 0$ (isothermal wall)

When the internal tube radius is small in comparison with the wave length and the radial velocity component, v, is small with respect to the axial velocity, u (*i.e.* $k < 1$ and $u/v < 1$), the basic equations can be reduced to:

$$i\tilde{u} = -\frac{1}{\gamma}\frac{\partial \tilde{p}}{\partial \xi} + \frac{1}{s^2}\left(\frac{\partial^2 \tilde{u}}{\partial \eta^2} + \frac{1}{\eta}\frac{\partial \tilde{u}}{\partial \eta}\right) \tag{B.26}$$

$$0 = -\frac{1}{\gamma}\frac{\partial \tilde{p}}{\partial \eta} \tag{B.27}$$

$$ik\tilde{\rho} = -\left[k\frac{\partial \tilde{u}}{\partial \xi} + \frac{\partial \tilde{v}}{\partial \eta} + \frac{\tilde{v}}{\eta}\right] \tag{B.28}$$

$$i\tilde{T} = \frac{1}{\sigma^2 s^2}\left[\frac{\partial^2 \tilde{T}}{\partial \eta^2} + \frac{1}{\eta}\frac{\partial \tilde{T}}{\partial \eta}\right] + i\frac{\gamma - 1}{\gamma}\tilde{p} \tag{B.29}$$

From the equation B.27 it can be seen that the amplitude of the pressure perturbation depends only on the axial coordinate ξ. Upon putting $\tilde{u} = f(\xi)h(z)$, with $z = i^{3/2}\eta s$. This way, equation B.26 can be

expressed as:

$$\frac{\partial^2 h}{\partial z^2} + \frac{1}{z}\frac{\partial h}{\partial z} + h = \frac{i}{\gamma f(\xi)}\frac{\partial \tilde{p}}{\partial \xi} \tag{B.30}$$

And its solution is given by:

$$h(z) = C_1 J_0(z) + C_2 Y_0(z) j + \frac{i}{\gamma f(\xi)}\frac{\partial \tilde{p}}{\partial \xi} \tag{B.31}$$

For u to be a finite value at $\eta = 0$, the constant C_2 must be zero. From the condition $\tilde{u} = 0$ for $\eta = 1$ it follows that:

$$f(\xi) = -\frac{i}{\gamma}\frac{1}{C_1 J_0(i^{3/2}s)}\frac{\partial \tilde{p}}{\partial \xi} \tag{B.32}$$

where from

$$\tilde{u} = f(\xi)h(z) = \frac{i}{\gamma}\frac{\partial \tilde{p}}{\partial \xi}\left[1 - \frac{J_0(i^{3/2}\eta s)}{J_0(i^{3/2}s)}\right] \tag{B.33}$$

Taking the same procedures for the temperature perturbation $\tilde{T}$, the solution that fulfils the requirement that $\tilde{T}$ remains finite for $\eta = 0$ and vanishes for $\eta = 1$ yields:

$$\tilde{T} = \frac{\gamma - 1}{\gamma}\tilde{p}\left[1 - \frac{J_0(i^{3/2}\sigma\eta s)}{J_0(i^{3/2}\sigma s)}\right] \tag{B.34}$$

substituting B.34 in B.16 gives:

$$\tilde{\rho} = \tilde{p}\left[1 - \frac{\gamma - 1}{\gamma}\left(1 - \frac{J_0(i^{3/2}\sigma\eta s)}{J_0(i^{3/2}\sigma s)}\right)\right] \tag{B.35}$$

Finally the equation of continuity has to be satisfied, thus:

$$\frac{1}{\eta}\frac{\partial(\tilde{v}\eta)}{\partial \eta} = k\left[i\tilde{\rho} + \frac{\partial \tilde{u}}{\partial x}\right] \tag{B.36}$$

Combining equations B.33 and B.35 into B.36:

$$\frac{1}{\eta}\frac{\partial(\tilde{v}\eta)}{\partial \eta} = ik\left[\tilde{p}\left[1 - \frac{\gamma - 1}{\gamma}\left(1 - \frac{J_0(i^{3/2}\sigma\eta s)}{J_0(i^{3/2}\sigma s)}\right)\right] + \frac{1}{\gamma}\frac{\partial^2 \tilde{p}}{\partial \xi^2}\left(1 - \frac{J_0(i^{3/2}\eta s)}{J_0(i^{3/2}s)}\right)\right] \tag{B.37}$$

After integration with respect to η:

$$\tilde{v}\eta = ik\left[\tilde{p}\left[\frac{1}{2}\eta^2 - \frac{\gamma - 1}{\gamma}\left(\frac{1}{2}\eta^2 - \frac{\eta}{i^{3/2}\sigma s}\frac{J_1(i^{3/2}\sigma\eta s)}{J_0(i^{3/2}\sigma s)}\right)\right] + \frac{1}{\gamma}\frac{\partial^2 \tilde{p}}{\partial \xi^2}\left(\frac{1}{2}\eta^2 - \frac{\eta}{i^{3/2}s}\frac{J_1(i^{3/2}\eta s)}{J_0(i^{3/2}s)}\right) + F(\xi)\right] \tag{B.38}$$

From the boundary condition $v = 0$ at $\eta = 1$:

$$-F(\xi) = \frac{1}{2}\tilde{p}\left[1 + \frac{\gamma - 1}{\gamma}\frac{J_2(i^{3/2}\sigma s)}{J_0(i^{3/2}\sigma s)} - \frac{1}{2\gamma}\frac{\partial^2 \tilde{p}}{\partial \xi^2}\frac{J_2(i^{3/2}s)}{J_0(i^{3/2}s)}\right] \tag{B.39}$$

Axial symmetry leads to $\lim_{\eta \to 0} v = 0$. This requirement is fulfilled if $F(\xi) = 0$:

$$\tilde{p}\left[1 + \frac{\gamma - 1}{\gamma}\frac{J_2(i^{3/2}\sigma s)}{J_0(i^{3/2}\sigma s)}\right] - \frac{1}{\gamma}\frac{\partial^2 p}{\partial \xi^2}\frac{J_2(i^{3/2}s)}{J_0(i^{3/2}s)} = 0 \tag{B.40}$$

Solving the last equation for $\tilde{p}$:

$$\tilde{p} = Ae^{\Gamma\xi} + Be^{-\Gamma\xi} \tag{B.41}$$

with

$$\Gamma = \sqrt{\frac{J_0(i^{3/2}s)}{J_2(i^{3/2}s)}}\sqrt{\frac{\gamma}{n}} \tag{B.42}$$

$$n = \left[1 + \frac{\gamma - 1}{\gamma}\frac{J_2(i^{3/2}\sigma s)}{J_0(i^{3/2}\sigma s)}\right]^{-1} \tag{B.43}$$

The solutions for the other acoustic variables become:

$$\tilde{u} = \frac{i\Gamma}{\gamma}\left[1 - \frac{J_0(i^{3/2}\eta s)}{J_0(i^{3/2}s)}\right]\left(Ae^{\Gamma\xi} - Be^{-\Gamma\xi}\right) \tag{B.44}$$

$$\tilde{v} = ik\left[\frac{1}{2}\eta\left(1 + \frac{J_2(i^{3/2}s)\gamma}{J_0(i^{3/2}s)n}\right) + \frac{\gamma - 1}{i^{3/2}\sigma s}\frac{J_1(i^{3/2}\sigma\eta s)}{J_0(i^{3/2}\sigma s)} - \frac{\gamma}{i^{3/2}\sigma s}\frac{J_1(i^{3/2}\sigma\eta s)}{J_0(i^{3/2}\sigma s)}\right]\left(Ae^{\Gamma\xi} - Be^{-\Gamma\xi}\right) \tag{B.45}$$

$$\tilde{\rho} = \left[1 - \frac{\gamma - 1}{\gamma}\left(1 - \frac{J_0(i^{3/2}\sigma\eta s)}{J_0(i^{3/2}\sigma s)}\right)\right]\left(A_1e^{\Gamma\xi} + B_1e^{-\Gamma\xi}\right) \tag{B.46}$$

$$\tilde{T} = \frac{\gamma - 1}{\gamma}\left[1 - \frac{J_0(i^{3/2}\sigma\eta s)}{J_0(i^{3/2}\sigma s)}\right]\left(A_1e^{\Gamma\xi} + B_1e^{-\Gamma\xi}\right) \tag{B.47}$$

The constants A and B can be determined by identifying additional boundary conditions at both ends of the tube. From the solution for the radial velocity v, it can be verified that the condition $u/v \ll 1$ is fulfilled if $k \ll 1$ and $k/s \ll 1$.